Ore Geology Reviews 142 (2022) 104570

Contents lists available at ScienceDirect

Ore Geology Reviews

journal homepage: www.elsevier.com/locate/oregeorev

Source and evolution of the ore-forming fluid of the Cuonadong Sn-W-Be polymetallic deposit (southern Tibet, China): Constraints from scheelite trace element and Sr isotope geochemistry

Zuo-Wen Dai [a], Guang-Ming Li [b,*], Yu-Ling Xie [a,*], Zhi-Ming Yang [a,c], Jan Marten Huizenga [d,e,f], Wei Liang [b], Jian-Gang Fu [b], Hua-Wen Cao [b]

[a] School of Civil and Resource Engineering, University of Science and Technology Beijing, Beijing 100083, China
[b] Chengdu Center, China Geological Survey, Chengdu 610081, China
[c] Institute of Geology, Chinese Academy of Geological Sciences, Beijing 100037, China
[d] Faculty of Environmental Sciences and Natural Resource Management, Norwegian University of Life Sciences, Postbox 5003, NO-1432, Ås, Norway
[e] Economic Geology Research Centre (EGRU), James Cook University, Townsville 4811, Australia
[f] Department of Geology, University of Johannesburg, PO Box 524, Auckland Park 2006, South Africa

ARTICLE INFO

Keywords:
Trace elements
Scheelite
Sr isotopes
Sn-W-Be polymetallic deposit
Cuonadong
Tibet
Himalaya

ABSTRACT

The Cuonadong Sn-W-Be polymetallic deposit is the first rare-metal deposit with an extraordinary metallogenic potential that has been discovered in the Tethyan Himalayan metallogenic belt. The deposit shows a wide range of different mineralization types, including greisen-, pegmatite-, skarn-, and hydrothermal vein-type mineralization. Of these mineralization types, the skarn-type has the largest inferred resources. In order to constrain the source and evolution of the ore-forming fluid, we conducted a detailed study of the skarn-hosted scheelite, including cathodoluminescence imaging, in-situ trace elemental analysis, and bulk Sr isotope analysis. In addition, bulk Sr isotope analysis of fluorite, phlogopite ^{40}Ar-^{39}Ar dating, and marble whole-rock geochemical analysis were also conducted. Phlogopite ^{40}Ar-^{39}Ar dating indicates that the skarn was formed at ca. 15 Ma, which is close to the formation age of the Cuonadong muscovite granite reported in previous studies. Cathodoluminescence images indicate that skarn-hosted scheelite can be subdivided into an older type 1 scheelite and a younger type 2 scheelite. Type 1 scheelite is characterized by a negative Eu anomaly, whereas type 2 scheelite shows a positive Eu anomaly. Considering the close temporal and spatial relationship between the Cuonadong Miocene leucogranite and the ore-bearing skarn, and their similar lanthanide tetrad effect as observed in the REE patterns, we propose that the negative Eu anomaly was inherited from the Cuonadong Miocene leucogranite, while the positive Eu anomaly resulted from the addition of Eu^{2+} to the ore-forming fluid during greisenization. Sr isotope data show that the fluorite $(^{87}Sr/^{86}Sr)_i$ value of 0.728885 is within the range of the Cuonadong Miocene leucogranite $(^{87}Sr/^{86}Sr)_i$ values, while scheelite $(^{87}Sr/^{86}Sr)_i$ values (0.709717–0.713480) are similar to those of the Cuonadong marble (0.709525–0.712146). Since scheelite is intergrown with fluorite, we propose that the hydrothermal fluid that exsolved from the Cuonadong Miocene leucogranite is responsible for formation of both fluorite and scheelite. Water-rock interaction between this magma-derived fluid and the marble is responsible for the loss of the scheelite magmatic Sr isotopic signature.

1. Introduction

Trace element geochemistry of hydrothermal minerals can constrain the composition and source of the ore-forming fluids from which they crystallized (Mukherjee, 2016, Zhao et al., 2018). Scheelite ($CaWO_4$) is an important tungsten-bearing ore or accessory mineral in different types of hydrothermal deposits such as porphyry-, quartz vein-, and skarn-type deposits (Brugger et al., 2000, 2008; Liu et al., 2007; Song et al., 2014; Fu et al., 2017a; Wissink et al., 2016; Fan et al., 2017; Sun and Chen, 2017; Zhang and Zhang, 2017; Poulin et al., 2018; Zhang

* Corresponding authors at: Chengdu Center, China Geological Survey, Jinniu District, Chengdu 610081, Sichuan Province, China (G.-M. Li). University of Science and Technology Beijing, Xueyuan Rd. 30, Haidian District, Beijing 100083, China (Y.-L. Xie).
E-mail addresses: 13982257109@163.com (G.-M. Li), yulinxie@ces.ustb.edu.cn (Y.-L. Xie).

https://doi.org/10.1016/j.oregeorev.2021.104570
Received 5 April 2021; Received in revised form 1 November 2021; Accepted 2 November 2021
Available online 8 November 2021

et al., 2018b; Zhao et al., 2018; Cao et al., 2020a). Spatially and temporally, scheelite is often associated with gold, pyrite, molybdenite, chalcopyrite, and cassiterite, making it an effective metallogenic indicator mineral (Ghaderi et al., 1999; Brugger et al., 2008; Wissink et al., 2016; Zhang and Zhang, 2017). Scheelite can incorporate relatively high concentrations of certain trace elements, e.g. Mo, Sr, Y, Pb, Nb, Na, and rare earth elements (REEs) via substitution of Ca^{2+} and W^{6+}. Scheelite trace element geochemistry can, therefore, provide essential information about the source, physico-chemical conditions, and evolution of ore-forming fluids (Ghaderi et al., 1999; Song et al., 2014; Mukherjee, 2016; Fan et al., 2017; Sun and Chen, 2017; Zhang et al., 2018b; Zhao et al., 2018; Cao et al., 2020b). In-situ laser ablation-inductively coupled plasma-mass spectrometry (LA-ICP-MS) has been widely adopted in analyzing trace element geochemical compositions of a variety of minerals (Brugger et al., 2000; Fu et al., 2017a; Mukherjee, 2016; Fan et al., 2017; Guo et al., 2018; Zhang et al., 2018b; Zeng et al., 2020). LA-ICP-MS has numerous advantages compared to digestion ICP-MS with regards to processing time, sample preparation, and spatial resolution (Wagner and Boyce, 2006). Therefore, LA-ICP-MS is a useful tool for scheelite elemental analysis, allowing us to better understand the genesis and ore formation of hydrothermal deposits. Additionally, the incorporation of Sr and rejection of Rb in scheelite makes Sr isotope an effective tracer for investigating the source and evolution of ore-forming fluids (Liu et al., 2007; Song et al., 2014; Fu et al., 2017a; Mukherjee, 2016; Sun and Chen, 2017; Zhang and Zhang, 2017).

In 2016, researchers from the Chengdu Centre (China Geological Survey) identified the Cuonadong gneiss dome in southern Tibet (Fu et al., 2017b, Fu et al., 2018a). This was followed by the discovery of the Cuonadong Sn-W-Be polymetallic deposit within the dome (Li et al., 2017). The Cuonadong deposit is the first rare-metal polymetallic deposit discovered in the Tethyan Himalayan Pb-Zn-Sb-Au metallogenic belt. It can be used as a case study to establish the relationship between the Cenozoic Himalayan leucogranites and rare-metal mineralization in the Tethyan Himalayan metallogenic belt. Previous studies mainly focused on the ore geology, geochronology, and the petrogenesis and evolution of the possibly related leucogranites (Fu et al., 2018b; Fu et al., 2020; Liang et al., 2018; Xie et al., 2018; 2020; Cao et al., 2020a; 2021; Xiang et al., 2020).

In this study, we conducted in-situ elemental analysis on skarn-hosted scheelite (main tungsten-bearing ore mineral in the deposit) and bulk Sr isotope analysis on scheelite and fluorite. This was supplemented by cathodoluminescence (CL) imaging, phlogopite ^{40}Ar-^{39}Ar dating, and whole-rock geochemistry of the marble. These data will shed a light on the source and evolution of the ore-forming fluid of the Cuonadong Sn-W-Be polymetallic deposit.

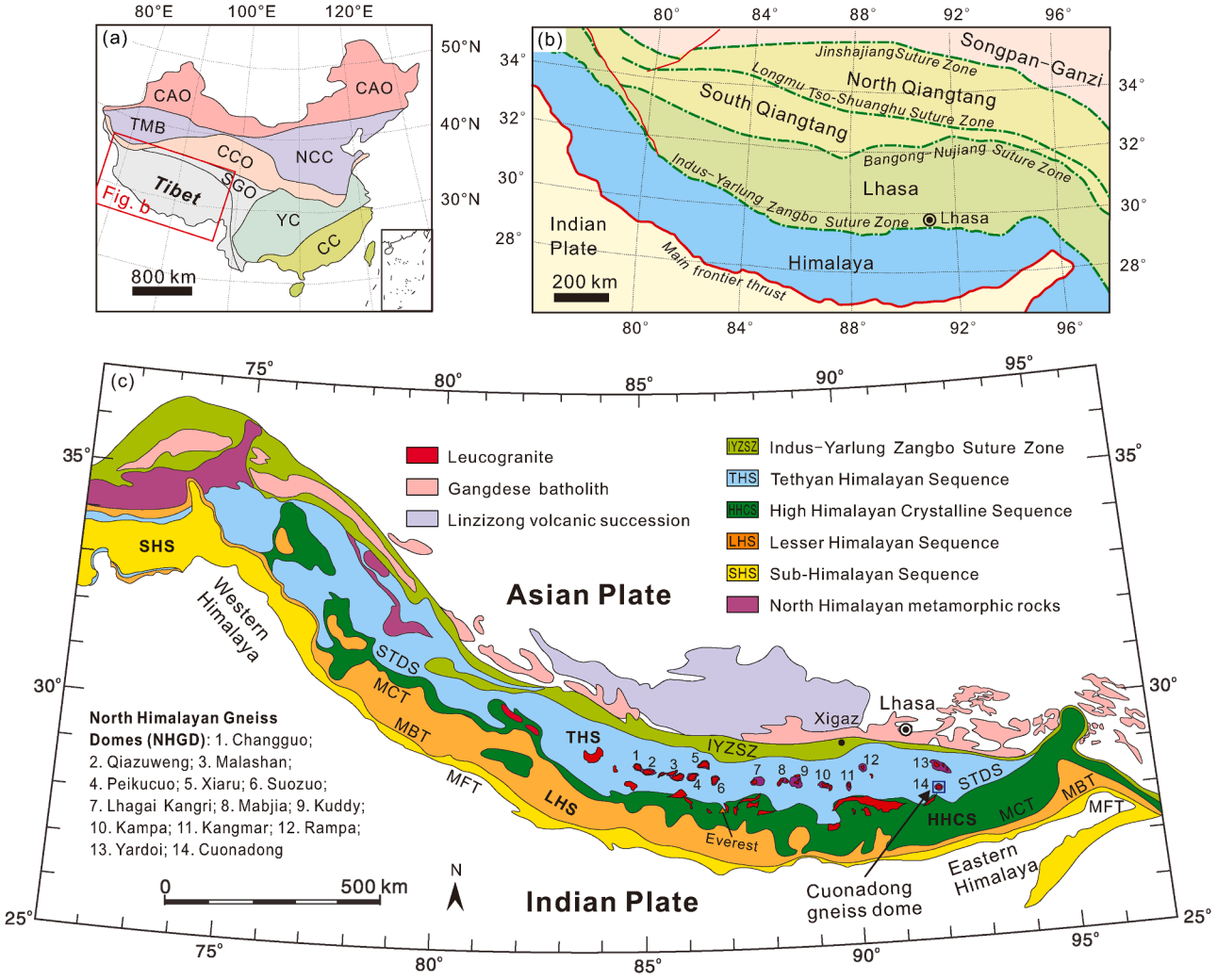

Fig. 1. (a) Tectonic division of China, showing the location of Tibet (modified after Pan et al., 2009). (b) The tectonic subdivision of the Tibet Plateau, showing the major sutures and terranes (modified after Yin and Harrison, 2000; Pan et al., 2012). (c) Simplified geological map of Himalaya showing the subdivision of Himalaya and distribution of Himalayan leucogranites (modified after Guillot et al., 2008; Dai et al., 2020; Zhang et al., 2020a). CAO: Central Asia Orogen; TMB: Tarim Block; NCC: North China Craton; CCO: Central China Orogen; SGO: Songpan Ganzi Orogen; YC: Yangtza Craton; CC: Cathaysia Craton.

2. Regional geological setting

The Himalayan-Tibetan Plateau, situated in western China (Fig. 1a), is a tectonic collage of five parallel E-W trending terranes. These include (from north to south) the Songpan-Ganzi, North Qiangtang, South Qiangtang, Lhasa, and Himalaya terranes (Fig. 1b, Yin and Harrison, 2000; Pan et al., 2012). The Himalaya terrane is separated from the Lhasa terrane by the Indus-Yarlung Zangpo Suture Zone and from the Indian Craton by the Main Frontier Thrust (Fig. 1c, Yin, 2006).

The Himalaya terrane can be subdivided into four litho-tectonic units (Fig. 1c, Yin, 2006), which include (from north to south): (1) The Tethyan Himalayan Sequence, which is predominantly composed of Paleozoic to Paleogene low-grade metamorphic siliclastic and carbonate rocks (Myrow et al., 2019). These Phanerozoic strata were deposited on the Indian passive continental margin (Cao et al., 2018) and host the Pb-Zn-Ag-Sb-Au deposits in the Himalaya terrane (Yang et al., 2009; Sun et al., 2016a); (2) The High Himalayan Crystalline Sequence comprising Late Proterozoic to Early Paleozoic upper amphibolite to lower granulite facies metamorphic rocks (Kohn, 2014; Mukherjee et al., 2019); (3) The Lesser Himalayan Sequence, which consists of Proterozoic greenschist to amphibolite facies metasedimentary rocks (Kohn, 2014), and (4) The Sub-Himalayan Sequence, which consists of Neogene alluvial sedimentary rocks that represent an overfilled stage of the Himalayan foreland basin. These subterranes are separated from each other by the South Tibetan detachment system, the Main Central Thrust, and the Main Boundary Thrust (Fig. 1c).

The Himalayan orogen is the product of the Cenozoic India-Eurasia collision (55 ± 10 Ma) following the closure of the Neo-Tethyan Ocean (Mo et al., 2007; An et al., 2021, Jain, 2014, Zheng and Wu, 2018). During this collision, the crust beneath this orogen experienced thickening and extensive anatexis (Zeng et al., 2009; 2012; Hou et al., 2012; Gao et al., 2016; Dai et al., 2020; Ji et al., 2020), resulting in the formation of Cenozoic leucogranites (Wu et al., 2015; 2020). These leucogranites formed two sub-parallel leucogranite belts, namely the Tethyan Himalayan leucogranite belt (also termed the North Himalayan leucogranite belt) to the north and the High Himalayan leucogranite belt to the south (Fig. 1c). The Himalayan leucogranites were emplaced over a prolonged period from 46 to 7 Ma (Wu et al., 2015; 2020). The Eocene leucogranites are commonly characterized by high Sr/Y ratios and, therefore, considered to be partial melting products of a thickened lower crust comprising amphibolite and subordinate metapelites of the High Himalayan Crystalline Sequence (Zeng et al., 2011; 2015; Hou et al., 2012; Dai et al., 2020). The Miocene leucogranites are highly fractionated peraluminous to strong peraluminous S-type granites (Wu et al., 2015; 2020) and have great potential for rare-metal mineralization (Li et al., 2017; Wang et al., 2017; Huang et al., 2019; Wu et al., 2020; Xie et al., 2020).

It is noteworthy that a series of gneiss domes occurring in the middle of the Tethyan Himalayan Sequence constitute the discontinuous beaded North Himalaya Gneiss Domes, which is a typical feature of the Tethyan Himalayan orogenic belt (Zhang et al., 2012; Fu et al., 2017b; Jessup et al., 2019). These domes are typically cored by amphibolite- to granulite-facies Early to Middle Palaeozoic (520–430 Ma) granitic gneisses (Gao et al., 2012, 2019; Zhang et al., 2019), and subordinate Neoproterozoic granitic gneisses (Xia et al., 2019), which were intruded by Eocene to Miocene two-mica granites or leucogranites (Wu et al., 2015; 2020). The cores of the Himalayan gneiss domes are separated from the overlying low-grade Tethyan Himalayan Sequence by north-trending detachment shear zones (Zhang et al., 2007; Fu et al., 2017b).

The North Himalayan Metallogenic Belt is an important component of the Tethys-Himalaya Metallogenic Domain (Yang et al., 2009; Zheng et al., 2014). This belt comprises Eocene and Miocene orogenic-type gold deposits, and hydrothermal vein-type Pb-Zn-Ag-Sb-Au deposits (eg., Cao et al., 2019; Yang et al., 2009; Zheng et al., 2014; Sun et al., 2016b; Zhang et al., 2020b). The discovery of the Cuonadong Sn-W-Be polymetallic deposit within the Cuonadong gneiss dome indicates that the North Himalayan Metallogenic Belt has prospecting potential for rare-metal deposits (Li et al., 2017).

3. Geology of the Cuonadong gneiss dome

The 400 km^2 sized, rhombus-shaped Cuonadong gneiss dome (Fig. 2, Dai et al., 2019; Cao et al., 2020a) is located in the eastern part of the North Himalaya Gneiss Domes, about 150 km to the east of the Kangmar Dome and 40 km to the south of Yardoi Dome (Fig. 1c, Fu et al., 2017b, 2018a, 2020). The dome comprises three lithological-tectonic units, i.e. (from core to rim) the lower, middle and upper unit. These units are separated from each other by a ductile lower detachment fault and a brittle upper detachment fault (Figs. 2, 3, 4a; Fu et al., 2017b, 2018a, 2020). The lower unit consists of Early Paleozoic augen orthogneiss (ca. 500 Ma; Figs. 2, 3, 4b, c; Zhang et al., 2019), and subordinate Neoproterozoic orthogneiss (ca. 810 Ma; Fig. 2; Xia et al., 2019), migmatite, amphibolite, paragneiss and sillimanite-bearing garnet-mica schist at the top (Fu et al., 2017b; 2020; Fu et al., 2018a). The middle unit predominately consists of strongly deformed schist (Figs. 2, 3, 4d), amphibolite, and quartzite interbedded with marble (Figs. 2, 3, 4e-h). The metamorphic grade increases downward as demonstrated by a typical Barrovian metamorphic sequence (i.e., biotite, garnet + staurolite, and garnet + kyanite + sillimanite zones) in the schist (Fu et al., 2017b; 2020; Fu et al., 2018a). The upper unit consists of Jurassic and minor Triassic low-grade metasedimentary rocks (phyllite, and slate) and sedimentary rocks (mudstone and siltstone) that belong to the Tethyan Himalayan Sequence (Figs. 2, 3, 4i; Fu et al., 2017b; 2020; Fu et al., 2018a).

Within the Cuonadong dome, voluminous leucogranites and pegmatites intruded the gneisses, schists and marbles in the core and the mantle (Fig. 2, 3, 4c, d, f-h, j). Based on deformation and mineral assemblages, these leucogranites can be divided into three types: (1) strong to weakly deformed two-mica granite; (2) undeformed garnet-bearing two-mica granite, and (3) undeformed garnet and tourmaline-bearing muscovite granite, tourmaline granite, and pegmatite (Dai et al., 2019; Huang, 2019; Cao et al., 2020a; Fu et al., 2020). These leucogranites and pegmatite were emplaced between 34 and 15 Ma (Huang et al., 2018; Zhang et al., 2018a; Fu et al., 2020; Xie et al., 2020; Cao et al., 2021). It is worth noting that at or near the contact zones between the leucogranite (especially the muscovite granite)/pegmatite and marble, skarns are well developed with variable W-Sn-Be mineralization, which mainly occur as belts (Figs. 3, 4e, j-m).

4. Ore deposit geology

4.1. General overview

The Cuonadong Sn-W-Be polymetallic deposit is situated in the Cuonadong gneiss dome (Li et al., 2017). The deposit is rich in Sn, W, Be, and F, and accompanied by numerous other ore metals, including Cs, Rb, Nb, Ta, Pb, Zn, Cu, Bi, Au, and Ag (Li et al., 2017; Liang et al., 2018; Cao et al., 2021). Four areas that show significant metallogenic potential are identified around the dome, including the Xianglin, Dongjie, Rina, and Changming areas (Fig. 2). The Xianglin area is characterized by numerous mineralization types and has large inferred resources. It has, therefore, recently been targeted for mineral exploration (Cao et al., 2021), which has indicated that the average Sn, WO_3, and BeO grades are 0.36%, 0.21%, and 0.08%, respectively. Early estimates suggest Sn, WO_3 and BeO resources of > 80,000 tons, > 50,000 tons, and > 34,000 tons, respectively (Li et al., 2017; Cao et al., 2021).

4.2. Characteristics of the skarn-type orebody in the Xianglin area

Four major mineralization types have been observed in the Xianglin area, i.e. pegmatite-type Be mineralization (Fig. 5a), greisen-type Sn mineralization (Fig. 5b), hydrothermal vein-type Sn-W-Be-F

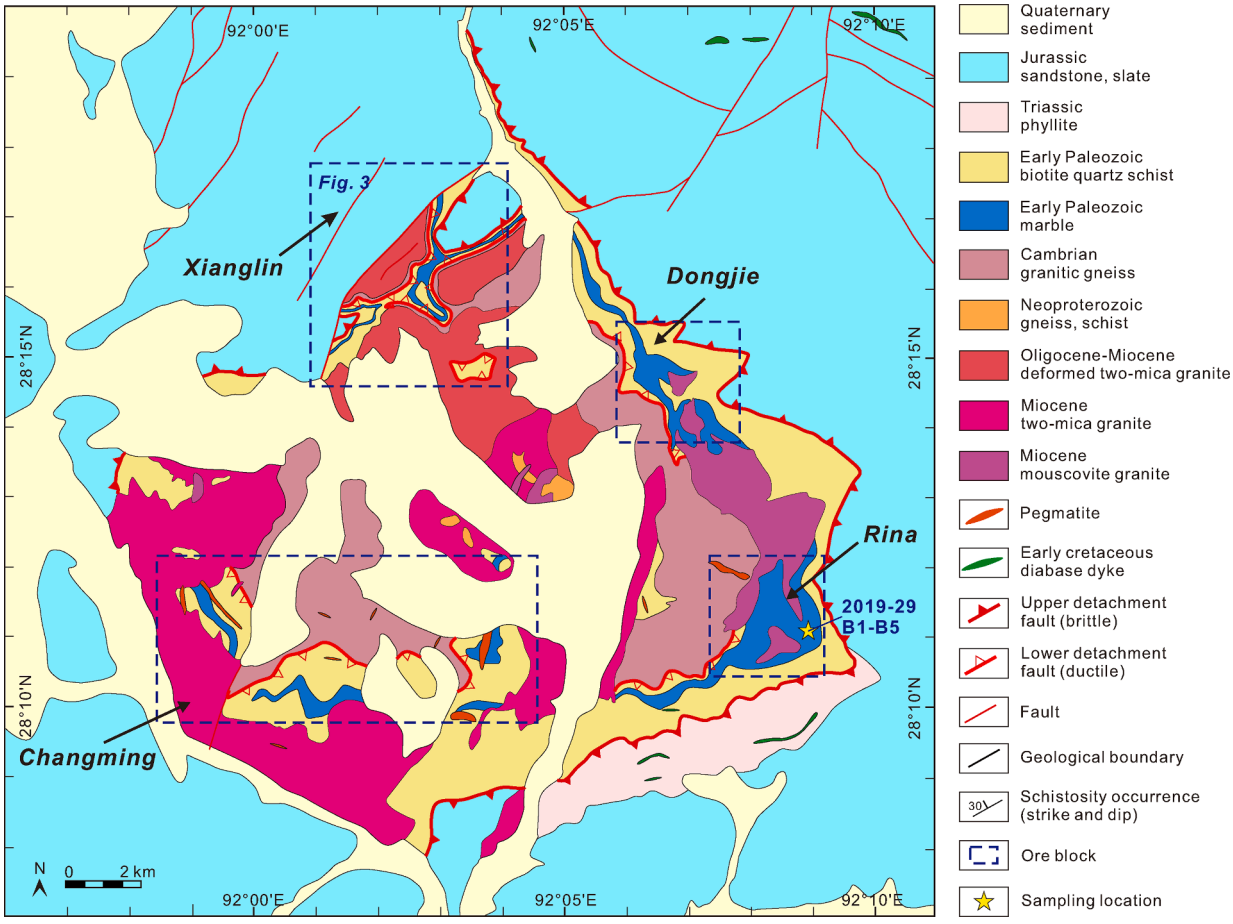

Fig. 2. Simplified geological map of the Cuonadong gneiss dome (modified after Xia et al., 2019, Cao et al., 2020a).

mineralization (Figs. 3, 5c), and skarn-type W-Sn-Be mineralization (Figs. 3, 4e, j-m, Fig. 5d-o). However, only the skarn- and hydrothermal vein-type orebodies have been delineated in this area (Fig. 3) and have large inferred WO_3 and BeO resources. The ore-forming potential of the pegmatite and greisen are unknown due to limited exploration.

As mentioned previously, the skarn-type W-Sn-Be mineralization is developed at or near the marble-leucogranite/pegmatite contact (Fig. 4j). These skarns are normally exposed in the outer contact zones (exoskarns) with widths ranging from several centimeters to tens of meters. In contrast, skarnization in the inner contact zones (endoskarn) is small in size (usually < 1 m) and weak in intensity. Generally, the skarn-type orebodies occur as belts extending for hundreds of meters up to ~ 3 km and with widths of 1–15 m (Fig. 3). Locally, the ores either appear as massive skarn (Fig. 4k), banded/ribbon skarn (Fig. 4l), or ethmoid skarn (Fig. 4m).

Ore minerals include scheelite (Fig. 5d-h, l-n), cassiterite (Fig. 5i, o), beryl (Fig. 5j), and phenacite (Fig. 5k). Gangue minerals include garnet, diopside, vesuvianite, wollastonite, tremolite, actinolite, chlorite, epidote, quartz, fluorite, calcite, tourmaline, muscovite, phlogopite, scapolite and sulfides (pyrrhotite, pyrite, chalcopyrite, sphalerite, and arsenopyrite) (Fig. 5d-o). Garnet, diopside, vesuvianite, wollastonite, and minor fluorite were formed during the prograde skarn stage (early stage), while tremolite, actinolite, chlorite, epidote, quartz, fluorite, calcite, tourmaline, and the sulfides were formed during the retrograde skarn stage (late stage) (Fig. 5d-o). The prograde skarn minerals are partly or completely replaced or crosscut by retrograde skarn minerals (Fig. 5j-n). The sub to -anhedral scheelite have a grain size of < 1 mm to 1 cm, and show a disseminated or taxitic texture (Fig. 5d-h, l-n). Eu- to suhedral cassiterite (0.2 mm to several millimeters in size) are randomly distributed within the skarn (Fig. 5i, o). Sub-to anhedral beryl and phenacite are 0.5–2 mm in size (Fig. 5j-k). The metallogenic stages and paragenetic sequence of minerals in the Cuonadong Sn-W-Be polymetallic deposit has been described in detail by Cao et al. (2021).

5. Sample collection and analytical methods

5.1. Sample collection and processing

Twelve samples (eight scheelite-bearing skarn and four marble samples) were collected from outcrops and exploratory trenches in Xianglin and Rina (Figs. 2, 3, Supplementary Table 1). All sample-processing procedures were conducted at the Langfang Regional Geological Survey (Hebei Province, China).

Skarn samples (D8036-B4, DZ372-B2, BT104-B4, BT119-B1, and D8036-B3) were crushed to 40 and 60 mesh, followed by screening, cleaning, drying, and magnetic separation. Scheelite, fluorite, and phlogopite separates (Supplementary Table 1) were selected using a binocular microscope. The single-mineral samples have purities of >99%. Pure scheelite and fluorite separates were ground in an agate mortar to 200 mesh fractions for Sr isotope analysis. The phlogopite separate was crushed and sieved to 60 and 80 mesh fractions and washed in distilled water and acetone for ^{40}Ar-^{39}Ar dating. Marble samples (2019-29B1 to 2019-29B4) were chipped and powdered to a mesh size of approximately 200 with a tungsten carbide ball mill for whole-rock trace element and Sr isotope analysis. Skarn samples (BT114-B5, BT113-B3, D8036-B1, and D8036-B3) were prepared as polished sections for CL imaging, electron microprobe analysis (EMPA), and laser ablation-inductively coupled plasma-mass spectrometric (LA-ICP-MS) analysis of scheelite.

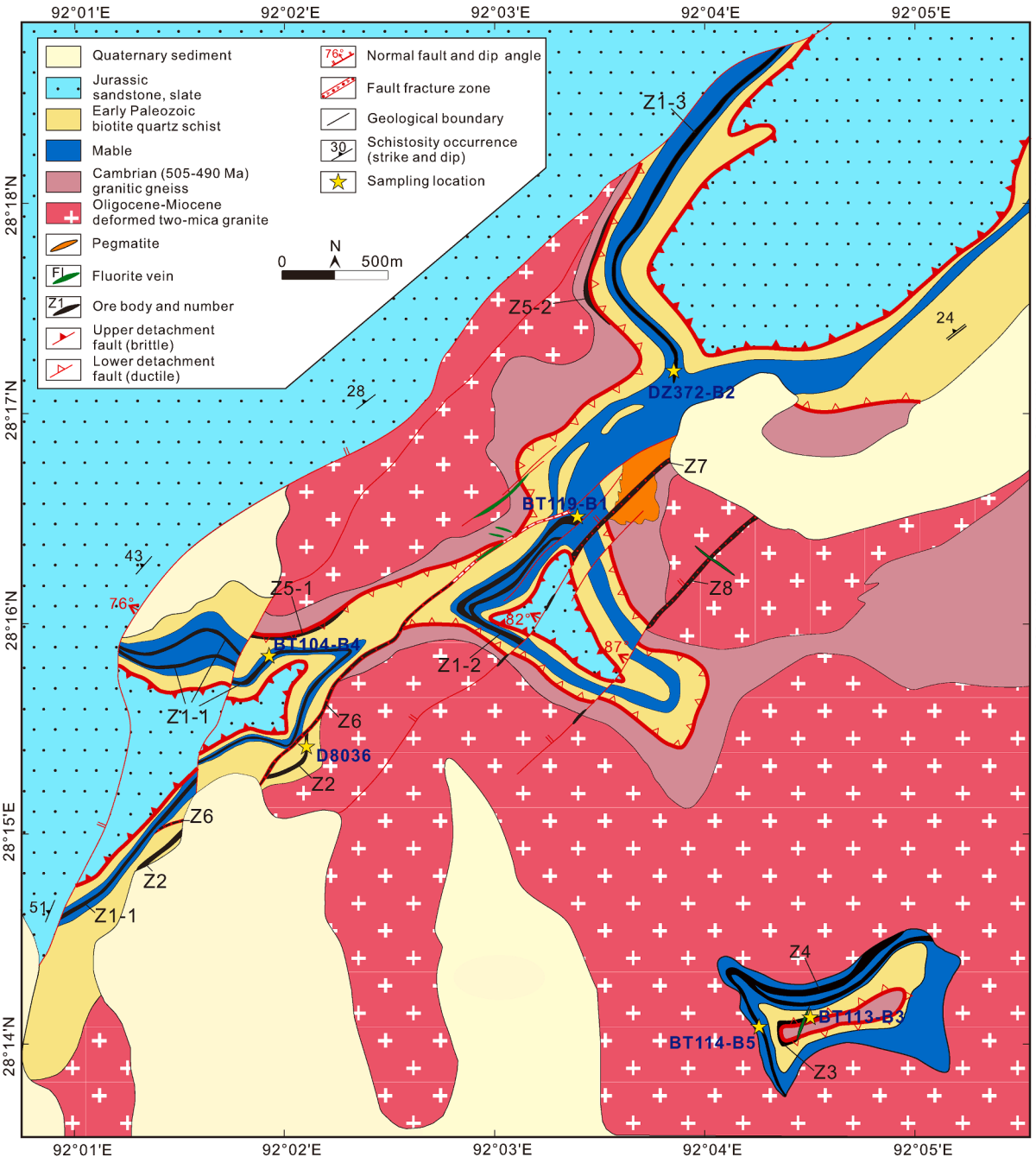

Fig. 3. Simplified geological map of the Xianglin area northwest of the Cuonadong dome (modified after Cao et al., 2020a).

5.2. Scheelite cathodoluminescence (CL) imaging

Scheelite CL imaging was conducted at the Advanced Analytical Centre, James Cook University (Townsville, Australia), on carbon-coated polished thin sections, using a JEOL JSM5410LV scanning electron microscope (SEM), fitted with a Robinson CL detector. Cathodeluminescence images were acquired at 20 kV acceleration voltage with a current of 6nA and a focused electron beam using the JEOL Semafore digital image acquisition software.

5.3. Scheelite electron microprobe analysis

Scheelite electron microprobe analysis was carried out at the Chengdu Center, China Geological Survey. Major element compositions of scheelite were obtained by wavelength dispersive spectrometry using an EMPA-1600 electron microprobe operating at an accelerating voltage of 15 kV with a 10nA beam current, a 1 μm beam diameter, and a 10–30 s counting time. Minerals and synthetic oxides were used as standards. All data were corrected using the ZAF procedure. The detection limit is 0.01% for most elements except for Mo and Ti (0.02%). The precision of all analyzed elements was better than 1.5%.

5.4. Bulk Rb-Sr isotope analysis of scheelite and fluorite

Scheelite and fluorite Sr isotopic compositions were determined using a PHOENIX thermal ionization mass spectrometer (TIMS) at the Beijing Research Institute of Uranium Geology, China. About 100 mg of scheelite or fluorite powder was completely dissolved in a mixture of HNO_3 + HF in a sealed Teflon beaker. Separation and purification of Rb and Sr were done using a second cation-exchange column, conditioned

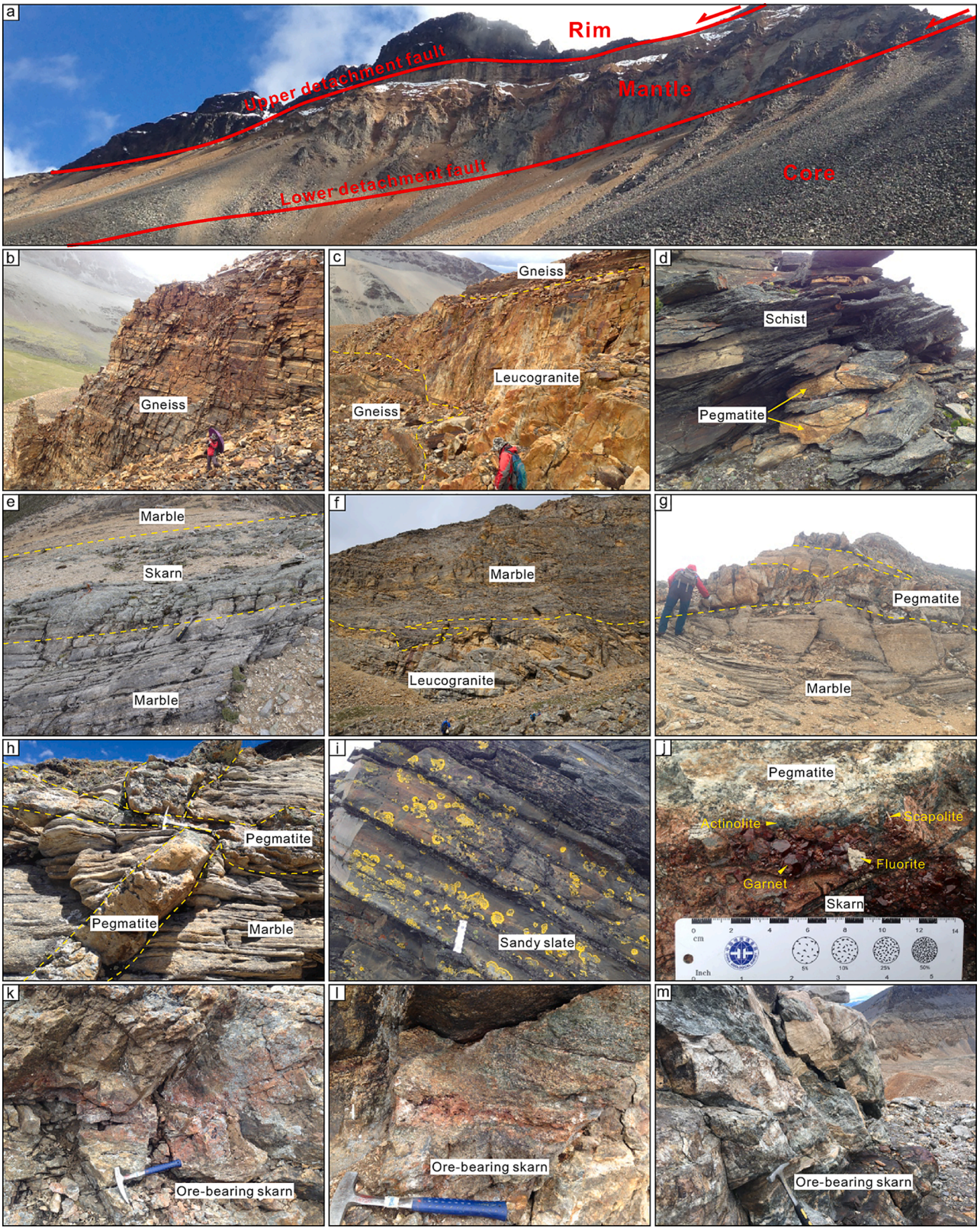

Fig. 4. Field photographs of the Cuonadong gneiss dome. (a) Macro outcrop showing the structure of the dome. (b) Macro outcrop of gneiss in the core of the dome. (c) Macro outcrop showing gneiss in the core was intruded by leucogranite. (d) Schist outcrop at the rim of the dome, which was intruded by pegmatite. (e) Outcrop of marble and skarn in the mantle of the dome. (f-h) Outcrops showing that the marble in the mantle of the dome was intruded by leucogranite or pegmatite. (i) Outcrop of sandy slate at the rim of the dome. (j) Outcrop showing the contact zone between the pegmatite and Cuonadong dome mantle experienced strong skarnization. (k-m) Outcrops of ore-bearing skarn in the mantle of the Cuonadong dome.

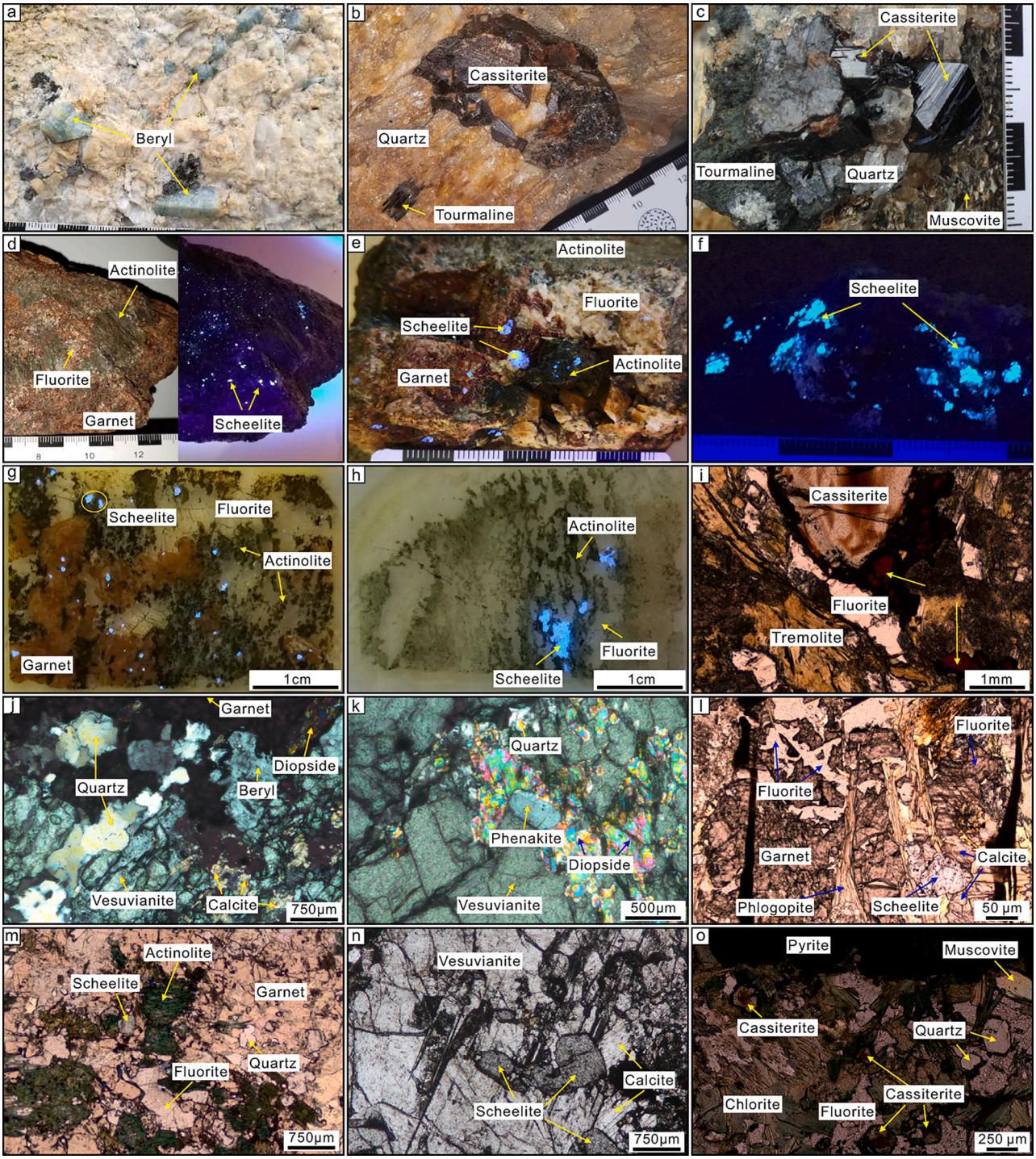

Fig. 5. Representative photographs of ores from the Cuonadong. (a) Beryl-bearing pegmatite. (b) Cassiterite-bearing greisen. (c) Cassiterite-bearing hydrothermal vein. (d-f) Representative photographs of skarn-type ores under ultraviolet light showing scheelite (distinct light blue color). (g-h) Microphotographs of skarn-type ores under ultraviolet light showing scheelite (distinct light-blue color). (i) Skarn-hosted subhedral cassiterite. (j-k) Quartz, beryl, phenakite, and calcite replacing the prograde skarn minerals garnet, diopside, and vesuvianite (crossed-polarized light). (l) Skarn-hosted scheelite intergrown with phlogopite, calcite, and fluorite (plane-polarized light). (m-o) Skarn-hosted scheelite and cassiterite intergrown with the retrograde skarn minerals actinolite, fluorite, quartz, chlorite, and muscovite replacing the prograde skarn minerals garnet and vesuvianite (plane-polarized light).

and cleaned with dilute HCl. Mass fractionation corrections for Sr isotopic ratios were based on a $^{86}Sr/^{88}Sr$ value of 0.1194. The reported $^{87}Sr/^{86}Sr$ ratios were adjusted to the Standard NBS SRM 987 $^{87}Sr/^{86}Sr = 0.710234 \pm 0.000006$ (2σ). The contents of Rb and Sr were measured using the isotope dilution method. The uncertainty in the concentration analyses by isotope dilution is 2% for Rb and 0.5–1% for Sr depending on the concentrations.

5.5. *^{40}Ar-^{39}Ar dating*

The phlogopite sample (D8036-B3; weight = 16.42 mg) was sealed into a quartz bottle for irradiation in a nuclear reactor (Swimming Pool Reactor, Chinese Institute of Atomic Energy, Beijing). The total time for irradiation was 1440 min, the neutron flux was about $2.65{\cdot}10^{13}$n cm^{-2} s^{-1}, and the integrated neutron flux was $2.29{\cdot}10^{18}$n cm^{-2}. The internal

Fangshan biotite (ZBH-25) standard with an age of 132.7 ± 1.2 Ma and a potassium content of 7.6 wt% was used in this study. The irradiation parameter J is 0.00253 ± 0.0000127.

The sample and standard were heated in a graphite furnace at a temperature range of 600-1230℃, and the heating extraction step for each temperature increment was 10 min with 20 min for purification. Mass analysis was carried out by multiple collector noble gas mass spectrometry using the Helix MC, and 20 sets of data were obtained for each peak value. The measured isotopic ratios were corrected for mass discrimination, atmospheric Ar component, blanks and irradiation-induced mass interference. The correction factors of interfering isotopes produced during irradiation were determined by analysis of irradiated pure K_2SO_4 and CaF_2, yielding the following ratios: $(^{36}Ar/^{37}Ar)_{Ca}$ = 0.0002389; $(^{40}K/^{39}Ar)_K$ = 0.004782; $(^{39}Ar/^{37}Ar)_{Ca}$ = 0.000806. The value of the decay constant (λ) that was used is 5.543×10^{-10} $year^{-1}$ (Steiger and Jäger, 1977). The Isoplot 3.75 software was adopted to calculate the plateau age and the generation of isochron and inverse isochron diagrams (Ludwig, 2012). The $^{40}Ar/^{39}Ar$ step-heating analysis was performed at the ^{40}Ar-^{39}Ar Laboratory, Institute of Geology, Chinese Academy of Geological Sciences (Beijing, China).

5.6. In-situ scheelite trace elements geochemistry

Representative scheelite grains in polished thin sections were analysed for trace elements using a laser ablation inductively coupled plasma mass spectrometry (LA-ICP-MS) system at the Advanced Analytical Centre at James Cook University. A Varian 820 quadrupole ICP mass spectrometer was coupled to a Geolas Pro 193 nm ArF excimer laser. A laser energy density of ~ 5 J/cm^2, repetition rates of 10 Hz, and a beam diameter 44 and 90 μm was used, depending on the scheelite grainsize, during analysis. For each analysis, a 30-s background signal was collected before the laser was switched on for 50 s ablation of the sample material. Helium was used as carrier gas, and argon as the make-up gas and mixed with the carrier gas via a Y-connector before entering the ICP. Every tenth spot analysis was followed by two NIST SRM 610 and NIST SRM 612 analyses to correct the time-dependent drift of sensitivity and mass discrimination of the ICP-MS. Reference glasses (GSD1G and GSE1G) were analyzed prior to and after the sample measurements. NIST SRM 610 and Ca concentration tested by EMPA were used as external and internal standards, respectively. While NIST SRM 612 was used as monitor.

5.7. Marble whole-rock trace element geochemistry

Bulk trace elements of marble samples were determined by Thermo Scientific X Series II ICPMS, employing the NexION300D mass spectrometer instrument after acid digestion of samples in Teflon bombs and dilution with 2% HNO_3 at the Beijing Research Institute of Uranium Geology (China). Rock standards of the GBW series were analyzed together with samples to check the external reproducibility. The analytical precision of this instrument is generally < 1% for elements with concentrations > 200 ppm and 1–3% for elements with concentrations < 200 ppm.

6. Results

6.1. Cathodoluminescence imaging

Two skarn-hosted scheelite types/generations are identified by CL imaging, namely type 1 scheelite that displays clear oscillatory zoning with some residual straight crystal planes and type 2 scheelite typically without obvious oscillatory zoning (Fig. 6). Type 1 scheelite occurs within type 2 scheelite and is partly or completely replaced by type 2 scheelite, indicating that the type 2 scheelite formed after type 1 scheelite.

6.2. Scheelite electron microprobe data

Twenty-nine scheelite electron microprobe analysis are shown in

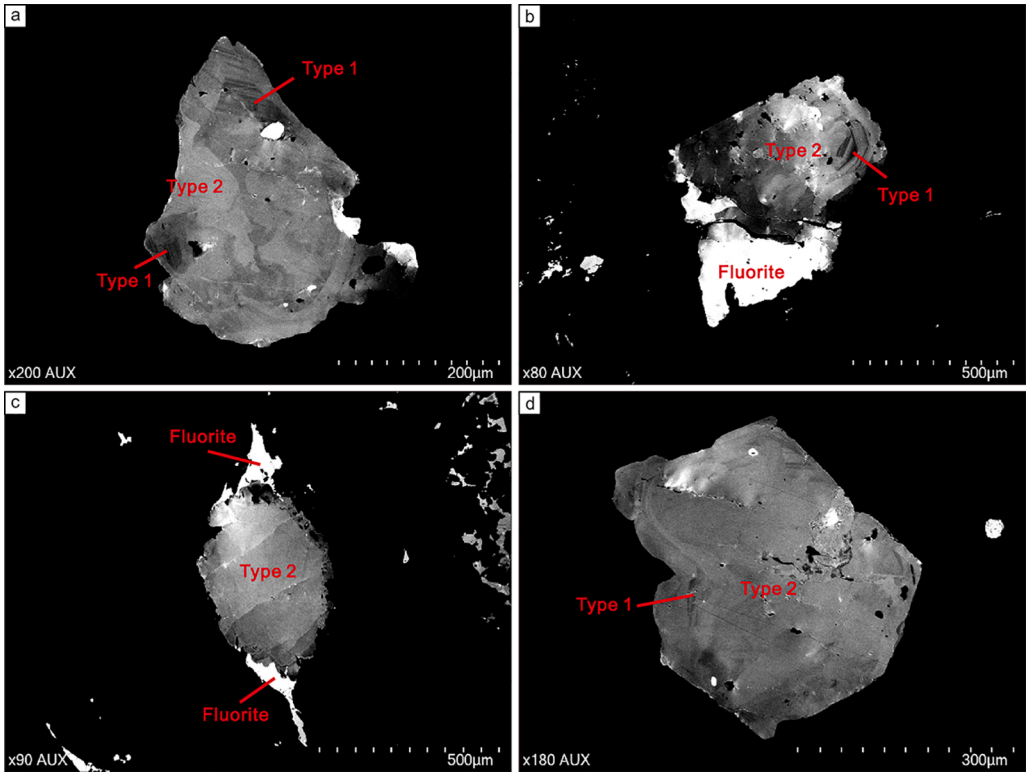

Fig. 6. Cathodeluminescence images of type 1 and 2 scheelite in the ore-bearing skarn from the Cuonadong Sn-W-Be polymetallic deposit.

Supplementary Table 2. The scheelite is characterized by high concentrations of CaO (15.99–17.90 wt%) and WO_3 (81.03–84.39 wt%), low MoO_3 (<0.38 wt%), and negligible concentrations of MnO, FeO, CuO, ZnO, and PbO.

6.3. Rb-Sr isotope compositions

The Sr isotope data of scheelite, fluorite and marble samples are listed in Supplementary Table 3. Scheelite samples have very low contents of Rb (0.82–1.25 ppm) but relatively high Sr contents (65.1–412.0 ppm). The $^{87}Rb/^{86}Sr$ ratios of the three scheelite samples range from 0.005963 to 0.038682 and the $^{87}Sr/^{86}Sr$ ratios range from 0.709719 to 0.713488 with $(^{87}Sr/^{86}Sr)_i$ values (normalized to 15 Ma) ranging from 0.709717 to 0.713480. Fluorite also has a low Rb (0.33 ppm) but a relatively high Sr content (30.5 ppm). The $^{87}Rb/^{86}Sr$ ratio of the fluorite sample is 0.031745 and the $^{87}Sr/^{86}Sr$ ratio is 0.728892 with a $(^{87}Sr/^{86}Sr)_i$ value (normalized to 15 Ma) of 0.728885. In contrast, the marble samples have relatively high Rb and Sr contents of 17.6–30.9 and 380–484 ppm, respectively. The $^{87}Rb/^{86}Sr$ ratios of the three marble samples are 0.105214–0.235339 and the $^{87}Sr/^{86}Sr$ ratios are 0.709547–0.712196 with $(^{87}Sr/^{86}Sr)_i$ values (normalized to 15 Ma) of 0.709525–0.712146.

6.4. Phlogopite ^{40}Ar-^{39}Ar age

The phlogopite ^{40}Ar-^{39}Ar dating result (sample D8036-B3) is listed in Supplementary Table 4 and illustrated in Fig. 7. The sample experienced eleven stages of heating from 600 to 1230℃, and yielded a ^{40}Ar-^{39}Ar plateau age of 15.16 ± 0.37 Ma (MSWD = 2.93) based on 82.9% of released ^{39}Ar, which was calculated from steps 6 to 11 (980-1230℃). The isochron age is 14.63 ± 1.22 Ma (MSWD = 3.09) with an intercept on the $^{40}Ar/^{36}Ar$ axis corresponding to the composition of atmospheric argon ($^{40}Ar/^{36}Ar$ = 303.9 ± 19.0), which is concordant with the plateau age. This age confirms the age dating results obtained by Cao et al. (2021).

6.5. Scheelite and marble trace element geochemistry

In-situ LA-ICP-MS trace element analytical results for scheelite and bulk trace element analytical results for marble are listed in Supplementary Table 5. Scheelite shows a variable Sr (26–165 ppm), Mo (10–282 ppm), Na (<0.01–211 ppm), Nd (1–10 ppm) and ΣREE (6–1667 ppm) contents. Scheelites have high LREE/HREE (0.8–26.5, average ratio of 5.7) and $(La/Yb)_N$ mass ratios (0.4–78.6, average ratio of 10.4), indicating LREE enrichment. The ΣREE (18–1667 ppm, average value of 208 ppm) content of type 1 scheelite are higher than the ΣREE content of type 2 scheelite (6–793 ppm, average value of 118 ppm). In addition, type 1 scheelite displays a weak to pronounced negative Eu anomaly with δEu [$\delta Eu = Eu_N/Eu^*_N$, where $Eu^*_N = (Sm_N \times Gd_N)^{1/2}$] ranging from 0.28 to 0.98 (average value of 0.55) (Fig. 8a; Supplementary Table 5). In contrast, the majority of type 2 scheelite display distinctly positive Eu anomalies with δEu values ranging from 1.00 to 11.13 (average value of 2.27) (Fig. 8b; Supplementary Table 5). Significantly, almost 67% of the analysed type 1 scheelite and>20% of the analysed type 2 scheelite have a $TE_{1,3}$ ($TE_{1,3} = [(Ce \times Pr \times Tb \times Dy)_N / (La \times Nd \times Gd \times Ho)_N]^{1/4}$) ≥ 1.1 (Supplementary Table 5), indicating a pronounced lanthanide tetrad effect ($TE_{1,3} > 1.1$) (Irber, 1999).

The four marble samples are, similar to scheelite, characterized by LREE enrichment and HREE depletion (LREE/HREE = 6–8, $(La/Yb)_N$ = 3–10) (Fig. 8; Supplementary Table 5). In addition, the marble samples show a negative Eu anomalies with δEu ranging from 0.46 to 0.53 (Fig. 8; Supplementary Table 5). Significantly, the marble samples do not show the lanthanide tetrad effect ($TE_{1,3}$ = 0.97–1.02) (Supplementary Table 5; Irber, 1999).

7. Discussion

7.1. Timing of mineralization

Phlogopite is a common accessory mineral that formed during retrograde skarn stage in the Cuonadong Sn-W-Be polymetallic deposit (Fig. 5l). This indicates that phlogopite in skarn formed almost simultaneously as scheelite. The phlogopite ^{40}Ar-^{39}Ar age, therefore, represents the mineralization age, which is at ca. 15 Ma (Fig. 7). This age is consistent with the age of the beryl-bearing pegmatite (muscovite ^{40}Ar-^{39}Ar age, ca. 15 Ma) and the ore-bearing hydrothermal vein (cassiterite U-Pb age, ca. 14.4 Ma) that crosscuts the skarn (Cao et al., 2020a). All these mineralization ages are very close to the formation age of Cuonadong muscovite granite (15.5 Ma; Cao et al., 2020a). It can, therefore, be concluded that the Cuonadong Sn-W-Be polymetallic deposit was formed at ca. 15 Ma and is related to the Cuonadong muscovite granite.

7.2. Mechanism for REE substitution into scheelite

Due to the similarity between ionic radii of REE^{3+} and that of Ca^{2+}, REEs can substitute for Ca in scheelite (Ghaderi et al., 1999). Importantly, the substitution of trivalent REEs for divalent Ca requires not only a modification of the crystal structure, particularly the size of the Ca site, but also a charge-compensating mechanism (Raimbault et al., 1993; Ghaderi et al., 1999). Studies have demonstrated that the following three mechanisms are considered to be the most important substitution mechanisms (Nassau and Loiacono, 1963; Burt, 1989;

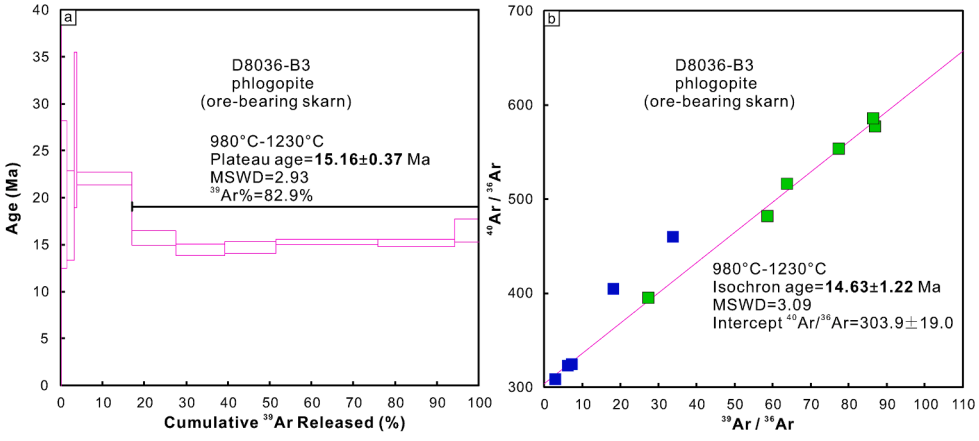

Fig. 7. (a) Phlogopite ^{40}Ar-^{39}Ar plateau age and (b) isochron age plots for ore-bearing skarn from the Cuonadong Sn-W-Be polymetallic deposit.

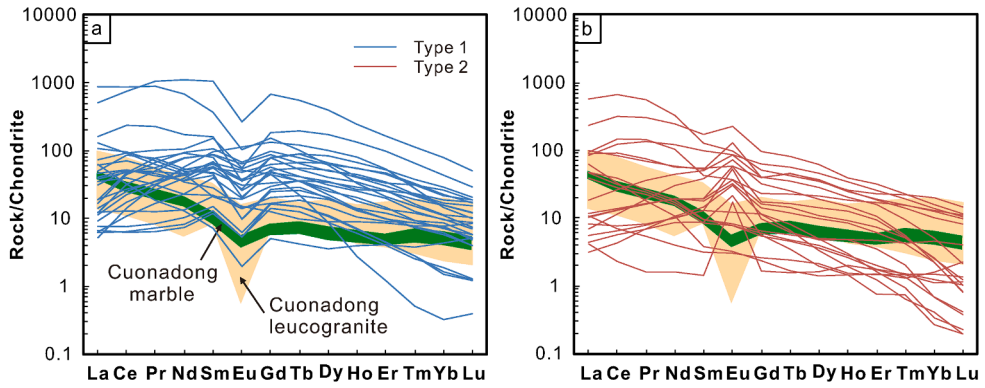

Fig. 8. Chondrite-normalized rare earth elements patterns for type 1 (a) and type 2 (b) scheelites in skarn from the Cuonadong Sn-W-Be polymetallic deposit. Whole-rock data of the Cuonadong leucogranite are from Huang (2019) and Dai (under review), the chondrite values are from Sun and McDonough (1989).

Ghaderi et al., 1999):

$$2Ca^{2+} = REE^{3+} + Na^{+} \quad (1)$$

$$Ca^{2+} + W^{6+} = REE^{3+} + Nb^{5+} \quad (2)$$

$$3Ca^{2+} = 2REE^{3+} + \square Ca \quad (3)$$

where □Ca denotes a Ca-site vacancy.

Typically, different substitution mechanisms will lead to distinct chondrite-normalized REE patterns of scheelite. If the Na content is sufficiently high in the ore-forming fluid, REEs with ironic radii close to 1.06 Å ($MREE^{3+}$) will preferentially substitute into the Ca (1.12 Å) site according to Eq. (1). Therefore, this substitution mechanism will lead to formation of scheelites characterized by a bell-shaped MREE-enriched REE pattern (Ghaderi et al., 1999; Brugger et al., 2002). Some scheelites show a convex upward REE pattern (Fig. 8), indicating that REEs probably did substitute into the Ca site according to Eq. (1). However, the majority of the scheelite samples show right-inclined REE patterns (Fig. 8). In addition, the ΣREE content of scheelite (ΣREE = 6–1667 ppm, average value of 169 ppm) is significantly higher than the Na content (3–211 ppm, average value of 28 ppm) (Supplementary Table 5). This suggests that the substitution mechanism according to Eq. (1) cannot be the main REE substitution mechanism into scheelite. This is also supported by the poor correlations between the ΣREE + Y-Eu, and the low Na contents (Fig. 9a).

According to the substitution mechanism represented by Eq. (2), scheelite should be enriched in Nb^{5+} and have Nb contents close to the ΣREE content. Dostal et al. (2009) proposed that this type of substitution

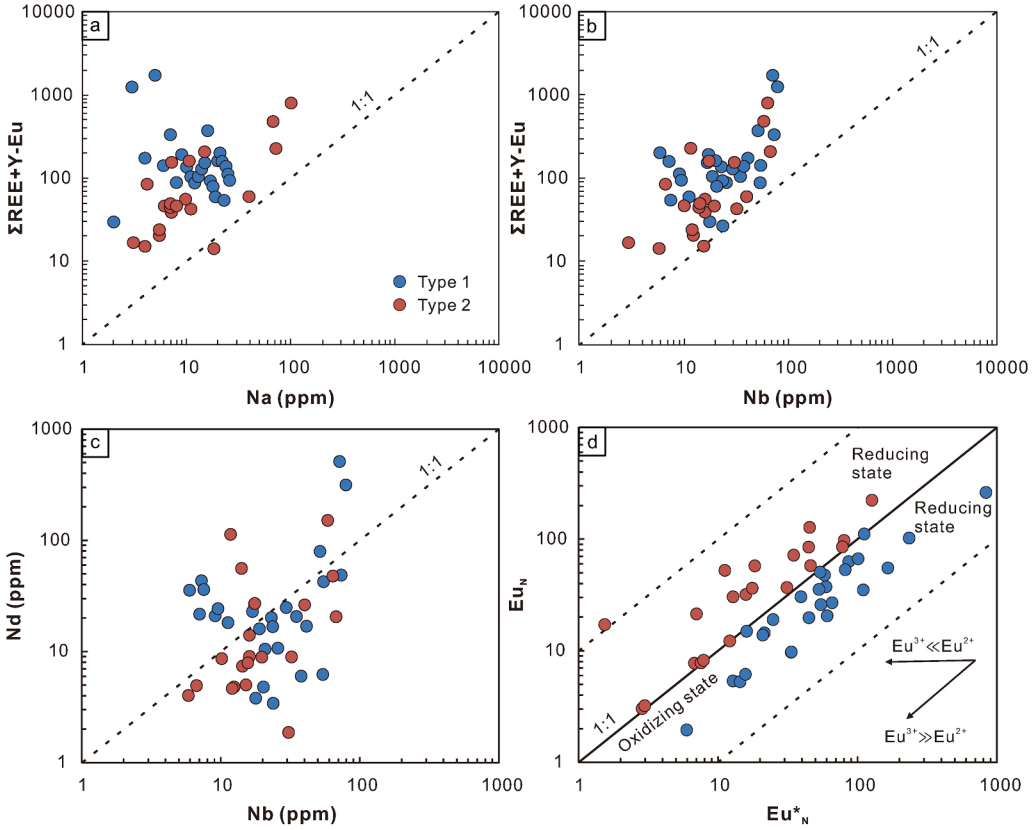

Fig. 9. (a) ΣREE + Y-Eu versus Na, (b) ΣREE + Y-Eu versus Nb, (c) Nd versus Nb, and (d) Eu_N versus Eu^*_N diagrams for skarn-hosted scheelite from the Cuonadong Sn-W-Be polymetallic deposit. (a), (b), and (d) are modified from Ghaderi et al. (1999). The dashed line in (d) represents δEu, where δEu = Eu_N/Eu^*_N and $Eu_N^* = (Sm_N \times Gd_N)^{1/2}$.

was responsible for the scheelite from the Nova Scotia deposit on the basis of a positive correlation between Nb^{5+} and Nd^{3+}. However, the skarn-hosted scheelite from the Cuonadong deposit has Nb content of 3–79 ppm (average value of 27 ppm), which is much lower than the ΣREE content (6–1667 ppm, average value of 169 ppm) (Supplementary Table 5). In addition, the large majority of the sample points deviate from 1:1 correlation line on the Nb vs. (ΣREE + Y-Eu) diagram (Fig. 9b) and no clear correlation between Nb and Nd is observed (Fig. 9c). Thus, substitution according to Eq. (2) is not likely to be the major substitution mechanism.

Therefore, REE substitution into scheelite can be best explained by the substitution mechanism described by Eq. (3). Typically, for this kind of substitution mechanism, REE ions substitute into the scheelite lattices in pairs related to a vacancy Ca site. It follows from Coulomb's law that the energy level for this substitution is minimized when the vacant Ca site lies between the two REE-substituted sites. The presence of such a vacancy adjacent to the REE sites allows them to be flexible. Thus, this substitution mechanism will remove the ionic radii restrictions and allow scheelites to incorporate REEs of any size (Ghaderi et al., 1999). Considering there is no priority for REE elements to substitute into Ca^{2+}, the scheelite will essentially inherit the REE characteristics of the ore-forming fluid.

7.3. Scheelite Eu anomalies

On the chondrite-normalized REE patterns, type 1 scheelite typically shows a pronounced negative Eu anomaly while type 2 scheelite commonly displays a remarkable positive Eu anomaly (Fig. 8). Studies have demonstrated that scheelite Eu anomalies are related to the redox conditions of the primary magmatic-hydrothermal fluid and fluid-rock interaction (Ghaderi et al., 1999; Brugger et al., 2008b; Song et al., 2014; Sun and Chen, 2017; Sun et al., 2019; Yuan et al., 2019; Cao et al., 2020b).

The ionic radius of Ca^{2+} is 1.12 Å, while those of Eu^{2+} and Eu^{3+} in scheelite (eightfold coordination) are 1.25 Å and 1.066 Å, respectively (Shannon, 1976). Therefore, both Eu^{2+} and Eu^{3+} can replace Ca in scheelite. However, since Eu^{2+} has an identical charge as Ca^{2+}, Eu^{2+} can substitute Ca in scheelite more easily under reducing conditions ($Eu^{2+} \gg Eu^{3+}$), resulting in a positive Eu anomaly. On the other hand, in an oxidizing environment, Eu occurs as Eu^{3+}, and shows similar behavior as the other REE^{3+}, thus resulting in no variation in the size of Eu anomalies (Ghaderi et al., 1999). Thus, negative Eu anomalies in type 1 scheelite may reflect oxidizing conditions, while positive Eu anomalies in type 2 scheelite may reflect reducing conditions. However, as will be discussed below, a variable redox state of ore-forming fluids is not likely to be the main factor that is responsible for the different Eu anomalies in type 1 and 2 scheelite.

A simple but effective model, proposed by Ghaderi et al. (1999) can be used to identity whether Eu^{2+} or Eu^{3+} dominates in scheelites utilizing ratios of Eu_N/Eu_N^* [here $Eu_N^* = (Sm_N \times Gd_N)^{1/2}$]. Type 1 scheelites mainly plot in the field between the 1:1 to 10:1 Eu_N/Eu_N^* ratio lines whereas type 2 scheelites mainly plot in the field between the 1:1 to 1:10 ratio lines (Fig. 9d), indicating that both type 1 and type 2 scheelite dominantly comprise Eu^{2+}, i.e. both scheelite types precipitated from reduced fluids (Ghaderi et al., 1999; Cao et al., 2020b).

Molybdenum may occur as Mo^{6+} and Mo^{4+} in fluids, the former being dominant in relatively oxidizing fluids while the latter occurs in reduced fluids (Bertine and Turekian, 1973). Considering the similar electron configuration and ionic radii, Mo^{6+} (0.62 Å) can substitute for W^{6+} (0.62 Å) in any proportion to form a complete solid solution between scheelite ($CaWO_4$) and powellite ($CaMoWO_4$) (Hsu and Galli, 1973; Tyson et al., 1988). In contrast, Mo^{4+} can hardly substitute for W^{6+}. Therefore, Mo concentrations in scheelite are relatively high in oxidizing conditions and low in reducing conditions. In addition, Mo contents will decrease dramatically if molybdenite precipitates under reduced conditions (Song et al., 2019; Sun et al., 2019). Thus, the scheelite Mo concentration is a suitable indicator for the ore-forming fluid redox state (Raimbault et al., 1993). Similarly, anomalies of the valence-variable element Ce can also been used to constrain the redox conditions of ore-forming fluids as Ce occurs as Ce^{4+} under oxidized conditions and Ce^{3+} under reduced conditions (Sun et al., 2019). Considering the charge balance during REE substitution into scheelites, Ce^{3+} would enter the scheelite lattices more easily compared to Ce^{4+}. Consequently, if the change of Eu anomalies in scheelites is induced by a variation of ore-forming fluid oxygen fugacity, positive correlations between δEu and Mo, and between δEu and δCe are expected (Sun et al., 2019). However, these correlations were not observed in scheelites (Fig. 10), which implies that a variation of the oxygen fugacity is less likely to be a controlling factor for the change of the Eu and Ce anomalies, and the Mo contents. The Mo concentrations of our samples (average value of 0.05 wt%) are much lower than those of the scheelites from other W deposits, e.g. the King Island skarn W deposit (Kwak and Tan, 1981), the Kara skarn W deposit (Zaw, 2000), and the Jitoushan and Baizhangyan W-Mo deposits (Song et al., 2014), suggesting that scheelites in this study precipitated from reduced fluids. This is supported by Raman microspectrometry of primary fluid inclusions in fluorite coexisting with scheelite, which show that N_2 and CH_4 are prevalent in these inclusions (Cao et al., 2021), confirming that a reduced fluid was related to tungsten mineralization.

Summarizing, it can be concluded that skarn-hosted scheelite were formed from a reduced fluids. This, however, is inconsistent with the negative Eu anomalies of type 1 scheelite (Fig. 8a). Since the substitution of REE^{3+} for Ca^{2+} in scheelites in this study is mainly controlled by the mechanism of Eq. (3), we propose that the Eu anomalies in type 1 scheelite were inherited from the ore-forming fluids that were depleted in Eu as observed in other deposits (Sun and Chen, 2017; Sun et al., 2019; Yuan et al., 2019; Cao et al., 2020b). The Cuonadong leucogranite and/or marble with pronounced Eu anomalies (Fig. 8) could be possible source for the ore-forming fluid due to their spatially close relationship with ore-bearing skarn (Fig. 11.).

It is noteworthy that the Eu depletion in the ore-forming fluid is inconsistent with the positive Eu anomaly in type 2 scheelite. The addition of Eu to the ore-forming fluid could have been an alternative explanation of the positive Eu anomalies in scheelites in reducing conditions. Variable scheelite Eu anomalies might be attributed to fluid-rock interaction (Brugger et al., 2002; Sun and Chen, 2017; Cao et al., 2020b). Intense fluid-rock interaction is supported by widespread skarnization and greisenization in the deposit. However, fluid-rock interaction between the primary ore-forming fluid and the marble (both of them have pronounced negative Eu anomalies) could not have led to the generation of scheelite with a positive Eu anomaly. In contrast, plagioclase in granite tends to be altered to sericite thereby supplying Eu^{2+} to the ore-forming fluid during greisenization (Sun and Chen, 2017). This process would enhance the Eu^{2+} concentration of the ore-forming fluids. Therefore, the addition of Eu^{2+} to the ore-forming fluids due to greisenization of the Cuonadong leucogranites was probably the main cause for the generation of a positive Eu anomaly in type 2 scheelite.

7.4. Source and evolution of ore-forming fluid

Ore-forming fluids for Sn-W deposits can either be fluids exsolved from highly evolved granites or metamorphic fluids from adjacent metamorphic rocks (Song et al., 2014, 2019; Sun and Chen, 2017; Sun et al., 2019; Yuan et al., 2019; Cao et al., 2020b). The main lithologies in the Cuonadong dome include Cambrian granitic gneiss in the core, marble and two-mica quartz schist in the mantle, and unmetamorphosed or slightly metamorphosed sedimentary rocks of the Tethyan Himalayan Sequence in the cover unit (Fig. 2). Thus, these lithologies could be possible fluid sources for the Cuonadong deposit. We evaluate their contributions to the deposit successively below.

Considering the close spatial and temporal relationships between the

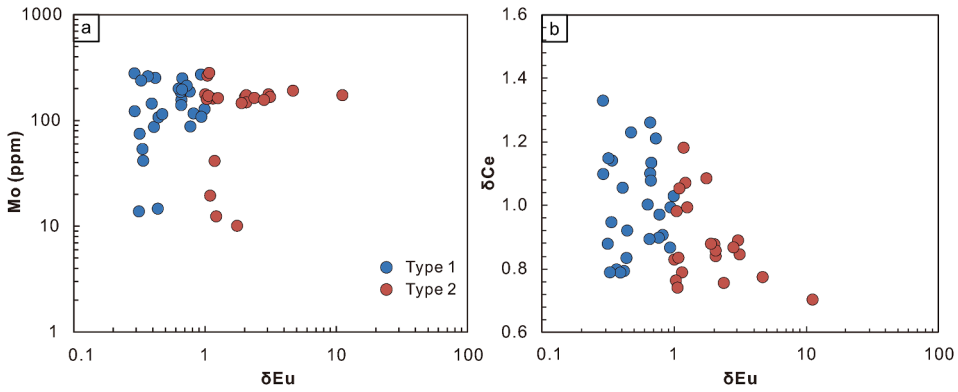

Fig. 10. (a) Mo versus δEu and (b) δCe versus δEu of skarn-hosted scheelite from the Cuonadong Sn-W-Be polymetallic deposit. $\delta Eu = Eu_N/Eu^*_N$, where $Eu^*_N = (Sm_N \times Gd_N)^{1/2}$ and $\delta Ce = Ce_N/(La_N \times Pr_N)^{1/2}$.

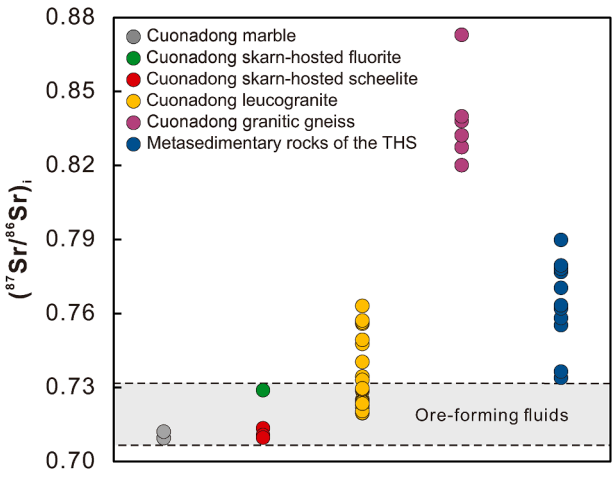

Fig. 11. Sr isotope composition of ore-forming fluids for skarn-type mineralization of the Cuonadong Sn-W-Be polymetallic deposit. The gray bar between the dotted lines represents the Sr isotopic features of ore-forming fluids, which range in between the Sr-isotope values of the Cuonadong leucogranite and marble. All initial $^{87}Sr/^{86}Sr$ ratios ($^{87}Sr/^{86}Sr)_i$ were recalculated to 15 Ma. Data of the Cuonadong granitic gneiss are from Zhang et al. (2019), data of metasedimentary rocks of the Tethyan Himalayan Sequence are from Richards et al. (2005), and data of the Cuonadong leucogranite are from Huang (2019) and Dai (unpublished data).

orebodies and Cuonadong leucogranite, this highly evolved leucogranite is very likely the source to ore-forming fluids. This is supported by their right-inclined chondrite-normalized REE patterns with pronounced negative Eu anomalies identical to those of type 1 scheelite (Fig. 8a). Additionally, the majority of analytical points of type 1 scheelite and 20% of analytical points of type 2 scheelite show pronounced lanthanide tetrad effect in the REE patterns (Fig. 8, Supplementary Table 5). Since REEs substituted for Ca^{2+} via Eq. (3), this lanthanide tetrad effect is inherited from ore-forming fluids. Studies have shown that garnet-bearing two-mica granite and garnet-bearing muscovite granite are characterized by remarkable lanthanide tetrad effect (Huang et al., 2018, Huang, 2019). This suggests that the primary ore-forming fluid was most likely derived from the Cuonadong leucogranite. Additionally, intergrown scheelite and fluorite is indicative of fluorine-rich ore-forming fluids. Fortunately, the Cuonadong leucogranite could be an ideal fluid source out of its fluorine-rich feature (Huang, 2019). Although marble in the mantle of Cuonadong dome is the major host rock for skarn-type orebodies, it is less likely to be the main fluid source due to lack of lanthanide tetrad effect on chondrite-normalized REE patterns (Fig. 8, Supplementary Table 5). Nevertheless, fluid-rock interaction between magma-derived ore-forming fluids and marble is probably the main cause for loss of the lanthanide tetrad effect for some of the scheelites.

The $(^{87}Sr/^{86}Sr)_i$ values of skarn-hosted fluorite is 0.728885, while $(^{87}Sr/^{86}Sr)_i$ values of skarn-hosted scheelite range between 0.709717 and 0.713480 (Supplementary Table 3). Both the fluorite and marble $(^{87}Sr/^{86}Sr)_i$ values are evidently lower than those of the Cuonadong granitic gneiss (0.820187–0.873031, Zhang et al., 2019) and the metasedimentary rocks of the Tethyan Himalayan Sequence (0.733955–0.789900, Richards et al., 2005) (all data were recalculated to 15 Ma). This implies that metamorphic fluids derived from these two lithologies can be excluded as a potential ore-forming fluid for the Cuonadong deposit.

Significantly, the $(^{87}Sr/^{86}Sr)_i$ value of the fluorite sample is within the range of the Cuonadong leucogranite $(^{87}Sr/^{86}Sr)_i$ values (0.719566–0.763132, Huang, 2019), whereas $(^{87}Sr/^{86}Sr)_i$ values of scheelite are similar to those of marble (0.709525–0.712146) (Supplementary Table 3) in the mantle of the Cuonadong dome. This implies that the fluorite-forming fluid represents a magmatic fluid exsolved from the Cuonadong leucogranite, whereas the scheelite-forming fluid was predominantly derived from metamorphic fluids from the marble. Evidently, this is inconsistent with the results of petrographic observation showing that fluorite and scheelite are intergrown (Fig. 5e, g-h, l, m, 7b, c). Therefore, we propose that the fluorite Sr isotope signature reflects the isotopic signature of a relatively primitive magmatic hydrothermal fluid, whereas the scheelite Sr isotope signature reflects the isotopic signature of an evolved magma-derived ore-forming fluid. Fluid-rock interaction can dramatically change the Sr isotopic features of scheelite and mask their Sr isotopic compositions of magmatic origin (Sun and Chen, 2017; Sun et al., 2019). Considering the similar Sr isotopic compositions of scheelite and marble, the more evolved fluid for scheelite was probably the result of intense fluid-rock interaction between the primitive magma-derived ore-forming fluid and the marble. This is consistent with the loss of the lanthanide tetrad effect of some of the scheelites. The supply of Ca from marble to the ore-forming fluids during fluid-rock interaction was one of the key controlling factors to scheelite precipitation in the deposit (Lecumberri-Sanchez et al., 2017). Further, the absence of wolframite [(Mn, Fe)WO_4] in the Cuonadong deposit indicates that the contribution of the two-mica quartz schist in mantle of the Cuonadong dome was negligible.

8. Conclusions

The results presented in this paper have led to the following conclusions:

(1) Phlogopite ^{40}Ar-^{39}Ar dating demonstrates that skarn-type mineralization of the Cuonadong Sn-W-Be polymetallic deposit occurred at ca. 15 Ma.

(2) The REEs of skarn-hosted scheelite from the Cuonadong Sn-W-Be polymetallic deposit were predominantly controlled by the substitution mechanism $3Ca^{2+} = 2REE^{3+} + \square Ca$. Therefore, the scheelite inherited the REE characteristics of the ore-forming fluid.

(3) Distinct Eu anomalies of type 1 and 2 scheelite, together with Sr isotopes, indicate that ore-forming fluid was a magmatic-hydrothermal fluid, which was geochemically and isotopically modified by intense fluid-rock interaction during skarnization and greisenization.

Declaration of competing interest

The authors declare that they have no known competing financial interests or personal relationships that could have influenced the work reported in this paper.

Acknowledgments

This paper is financially supported by the National Natural Science Foundation of China (91955208 and 41930427). We are grateful to Editor-in-Chief Huayong Chen, and two anonymous reviewers for their constructive comments and suggestions that significantly helped to improve the original manuscript.

Appendix A. Supplementary data

Supplementary data to this article can be found online at https://doi.org/10.1016/j.oregeorev.2021.104570.

References

An, W., Hu, X.M., Garzanti, E., Wang, J.G., Liu, Q., 2021. New precise dating of the India-Asia Collision in the Tibetan Himalaya at 61 Ma. Int. J. Earth Sci. 48, 1–10.

Bertine, K.K., Turekian, K.K., 1973. Molybdenum in marine deposits. Geochim. Cosmochim. Acta. 37 (6), 1415–1434.

Brugger, J., Etschmann, B., Pownceby, M., Liu, W., Grundler, P., Brewe, D., 2008. Oxidation state of europium in scheelite: tracking fluid-rock interaction in gold deposits. Chem. Geol. 257 (1-2), 26–33.

Brugger, J., Lahaye, Y., Costa, S., Lambert, D., Bateman, R., 2000. Inhomogeneous distribution of REE in scheelite and dynamics of Archaean hydrothermal systems (Mt. Charlotte and Drysdale gold deposits, Western Australia). Contrib. Mineral. Petr. 139 (3), 251–264.

Brugger, J., Maas, R., Lahaye, Y., McRae, C., Ghaderi, M., Costa, S., Lambert, D., Bateman, R., Prince, K., 2002. Origins of Nd-Sr-Pb isotopic variations in single scheelite grains from Archaean gold deposits, Western Australia. Chem. Geol. 182 (2-4), 203–225.

Burt, D.M., 1989. Compositional and phase relations among rare earth element minerals. Geochem. Miner. Rare Earth Elem. 21, 260–307.

Cao, H., Huang, Y., Li, G., Zhang, L., Wu, J., Dong, L., Dai, Z., Lu, L., 2018. Late Triassic sedimentary records in the northern Tethyan Himalaya: Tectonic link with Greater India. Geosci. Front. 9 (1), 273–291.

Cao, H.-W., Zou, H., Bagas, L., Zhang, L.-K., Zhang, Z., Li, Z.-Q., 2019. The Laqiong Sb-Au deposit: implications for polymetallic mineral systems in the Tethys-Himalayan zone of southern Tibet, China. Gondwana Res. 72, 83–96.

Cao, H.-W., Li, G.-M., Zhang, Z., Zhang, L.-K., Dong, S.-L., Xia, X.-B., Liang, W., Fu, J.-G., Huang, Y., Xiang, A.-P., Qing, C.-S., Dai, Z.-W., Pei, Q.-M., Zhang, Y.-H., 2020a. Miocene Sn polymetallic mineralization in the Tethyan Himalaya, southeastern Tibet: a case study of the Cuonadong deposit. Ore Geol. Rev. 119, 103403. https://doi.org/10.1016/j.oregeorev.2020.103403.

Cao, J., Yang, X., Zhang, D., Yan, F., 2020b. In situ trace elements and Sr isotopes in scheelite and S-Pb isotopes in sulfides from the Shiweidong W-Cu deposit, giant Dahutang ore field: implications to the fluid evolution and ore genesis. Ore Geol. Rev. 125, 103696. https://doi.org/10.1016/j.oregeorev.2020.103696.

Cao, H.-W., Li, G.-M., Zhang, R.-Q., Zhang, Y.-H., Zhang, L.-K., Dai, Z.-W., Zhang, Z., Liang, W., Dong, S.-L., Xia, X.-B., 2021. Genesis of the Cuonadong tin polymetallic deposit in the Tethyan Himalaya: evidence from geology, geochronology, fluid inclusions and multiple isotopes. Gondwana Res. 92, 72–101.

Dai, Z., Dong, L., Li, G., Huizenga, J.M., Ding, J., Zhang, L., Huang, Y., Cao, H., Lu, L., Yan, G., Santosh, M., 2020. Crustal thickening prior to 43 Ma in the Himalaya: evidence from lower crust-derived adakitic magmatism in Dala, eastern Tethyan Himalaya. Tibet. Geol. J. 55 (5), 4021–4046.

Dai, Z.W., Li, G.M., Ding, J., Zhang, L., Cao, H., Zhang, Z., Liang, W., 2019. Chemical and boron isotopic composition, and significance of tourmaline from the Cuonadong tourmaline granite. Tibet. Earth Sci. 44, 1849–1859 (in Chinese with English abstract).

Dostal, J., Kontak, D.J., Chatterjee, A.K., 2009. Trace element geochemistry of scheelite and rutile from metaturbidite-hosted quartz vein gold deposits, Meguma Terrane, Nova Scotia, Canada: genetic implications. Miner. Petrol. 97 (1-2), 95–109.

Fan, J.-J., Li, C., Wang, M., Liu, Y.-M., Xie, C.-M., 2017. Remnants of a Late Triassic ocean island in the Gufeng area, northern Tibet: implications for the opening and early evolution of the Bangong-Nujiang Tethyan Ocean. J. Asian Earth Sci. 135, 35–50.

Fu, Y.u., Sun, X., Zhou, H., Lin, H., Jiang, L., Yang, T., 2017a. In-situ LA-ICP-MS trace elements analysis of scheelites from the giant Beiya gold-polymetallic deposit in Yunnan Province, Southwest China and its metallogenic implications. Ore Geol. Rev. 80, 828–837.

Fu, J., Li, G., Wang, G., Huang, Y., Zhang, L., Dong, S., Liang, W., 2017b. First field identification of the Cuonadong dome in southern Tibet: implications for EW extension of the North Himalayan gneiss dome. Int. J. Earth Sci. 106 (5), 1581–1596.

Fu, J., Li, G., Wang, G., Zhang, L., Liang, W., Zhang, X., Jiao, Y., Dong, S., Huang, Y., 2020. Structural analysis of sheath folds and geochronology in the Cuonadong Dome, southern Tibet, China: new constraints on the timing of the South Tibetan Detachment System and its relationship to North Himalayan Gneiss Domes. Terra Nova 32 (4), 300–323.

Gao, L.-E., Zeng, L., Gao, J., Shang, Z., Hou, K., Wang, Q., 2016. Oligocene crustal anatexis in the Tethyan Himalaya, southern Tibet. Lithos 264, 201–209.

Gao, L.-E., Zeng, L., Hu, G., Wang, Y., Wang, Q., Guo, C., Hou, K., 2019. Early Paleozoic magmatism along the northern margin of East Gondwana. Lithos 334-335, 25–41.

Gao, L.E., Zeng, L.S., Xie, K.J., 2012. Eocene high grade metamorphism and crustal anatexis in the North Himalaya Gneiss Domes, Southern Tibet. Chinese Sci. Bull. 57 (6), 639–650.

Ghaderi, M., Palin, J.M., Campbell, I.H., Sylvester, P.J., 1999. Rare earth element systematics in scheelite from hydrothermal gold deposits in the Kalgoorlie-Norseman region, Western Australia. Econ. Geol. 94, 423-437.

Guillot, S., Mahéo, G., de Sigoyer, J., Hattori, K.H., Pêcher, A., 2008. Tethyan and Indian subduction viewed from the Himalayan high- to ultrahigh-pressure metamorphic rocks. Tectonophysics 451 (1-4), 225–241.

Guo, J., Zhang, R., Li, C., Sun, W., Hu, Y., Kang, D., Wu, J., 2018. Genesis of the Gaosong Sn-Cu deposit, Gejiu district, SW China: Constraints from in situ LA-ICP-MS cassiterite U-Pb dating and trace element fingerprinting. Ore Geol. Rev. 92, 627–642.

Hou, Z.-Q., Zheng, Y.-C., Zeng, L.-S., Gao, L.-E., Huang, K.-X., Li, W., Li, Q.-Y., Fu, Q., Liang, W., Sun, Q.-Z., 2012. Eocene-Oligocene granitoids in southern Tibet: Constraints on crustal anatexis and tectonic evolution of the Himalayan orogen. Earth Planet. Sci. Lett. 349-350, 38–52.

Hsu, L., Galli, P., 1973. Origin of the Scheelite-Powellite Series of Minerals. Econ. Geol. 68, 681-696.

Huang, C.M., 2019. Petrogenesis of the Cuonadong-Lhozag leucogranites and implication for tectonic evolution and Be-W-Sn metallogeny in southern Tibet. Doctoral thesis. China University of Geosciences (Beijing). (in Chinese with English abstract).

Huang, C.M., Li, G.M., Zhang, Z., Liang, W., Huang, Y., Zhang, L.K., Fu, J.G., 2018. Petrogenesis of the Cuonadong leucogranite in south Tibet: constraints from bulk-rock geochemistry and zircon U-Pb dating. Earth Sci. Front. 25, 182–195 (in Chinese with English abstract).

Huang, Y., Fu, J.G., Li, G.M., Zhang, L.K., Liu, H., 2019. Determination of Lalong Dome in South Tibet and New Discovery of Rare Metal Mineralization. Earth Sci. 44, 2197–2206 (in Chinese with English abstract).

Irber, W., 1999. The lanthanide tetrad effect and its correlation with K/Rb, Eu/Eu*, Sr/Eu, Y/Ho, and Zr/Hf of evolving peraluminous granite suites. Geochim. Cosmochim. Acta. 63 (3-4), 489–508.

Jain, A.K., 2014. When did India-Asia collide and make the Himalaya? Current Sci. 106, 254–266.

Jessup, M.J., Langille, J.M., Diedesch, T.F., Cottle, J.M., 2019. Gneiss dome formation in the Himalaya and southern Tibet. Geol. Soc. Lond. Spec. Publ. 483 (1), 401–422.

Kohn, M.J., 2014. Himalayan metamorphism and its tectonic implications. Annu. Rev. Earth Planet. Sci. 42 (1), 381–419.

Kwak, T.A.P., Tan, T.H., 1981. The geochemistry of zoning in skarn minerals at the King Island (Dolphin) Mine. Econ. Geol. 76, 468-497.

Lecumberri-Sanchez, P., Vieira, R., Heinrich, C.A., Pinto, F., Wälle, M., 2017. Fluid-rock interaction is decisive for the formation of tungsten deposits. Geology 45 (7), 579–582.

Li, G.M., Zhang, L.K., Jiao, Y.J., Xia, X.B., Dong, S.L., Fu, J.G., Liang, W., Zhang, Z., Wu, J.Y., Dong, L., Huang, Y., 2017. First discovery and implications of Cuonadong superlarge Be-W-Sn polymetallic deposit in Himalayan metallogenic belt, southern Tibet. Miner. Deposits 36, 1003–1008 (in Chinese with English abstract).

Liang, W., Zhang, L.K., Xia, X.B., Ma, G.T., Huang, Y., Zhang, Z., Fu, J.G., Cao, H.W., Miao, H.Q., Li, G.M., 2018. Geology and preliminary mineral genesis of the Cuonadong W-Sn polymetallic deposit, southern Tibet. China. Earth Sci. 43, 2742–2754 (in Chinese with English abstract).

Liu, Y., Deng, J., Li, C., Shi, G., Zheng, A., 2007. REE composition in scheelite and scheelite Sm-Nd dating for the Xuebaoding W-Sn-Be deposit in Sichuan. Chinese Sci. Bull. 52 (18), 2543–2550.

Ludwig, K.R., 2012. User's Manual for Isoplot 3.75: A Geochronological Toolkit for Microsoft Excel. Berkeley Geochronology Center, pp. 70.

Mo, X.X., Zhao, Z.D., Zhou, S.D.G.C., Dong, G.C., Liao, Z.L., 2007. On the timing of India-Asia continental collision. Geol. Bull. China 26, 1240–1244 (in Chinese with English abstract).

Mukherjee, P.K., Jain, A.K., Singhal, S., Singha, N.B., Singh, S., Kumud, K., Seth, P., Patel, R.C., 2019. U-Pb zircon ages and Sm-Nd isotopic characteristics of the Lesser and Great Himalayan sequences, Uttarakhand Himalaya, and their regional tectonic implications. Gondwana Res. 75, 282–297.

Mukherjee, S., 2016. Review on symmetric structures in ductile shear zones. Int. J. Earth Sci. 1–16.

Myrow, P.M., Fike, D.A., Malmskog, E., Leslie, S.A., Zhang, T., Singh, B.P., Chaubey, R.S., Prasad, S.K., 2019. Ordovician-Silurian boundary strata of the Indian Himalaya: Record of the latest Ordovician Boda event. Geol. Soc. Am. Bull. 131, 881-898.
Nassau, K., Loiacono, G.M., 1963. Calcium tungstate—III: Trivalent rare earth substitution. J. Phys. Chem. Solids. 24 (12), 1503–1510.
Pan, G., Wang, L., Li, R., Yuan, S., Ji, W., Yin, F., Zhang, W., Wang, B., 2012. Tectonic evolution of the Qinghai-Tibet Plateau. J. Asian Earth Sci. 53, 3–14.
Pan, G.T., Xiao, Q.H., Lu, S.N., Deng, J.F., Feng, Y.M., Zhang, K.X., Zhang, Z.Y., Wang, F. G., Xing, G.F., Hao, G.J., Feng, Y.F., 2009. Subdivision of tectonic units in China. Geol. China. 36, 1–28 (in Chinese with English abstract).
Poulin, R.S., Kontak, D.J., McDonald, A., McCLenaghan, M.B., 2018. Assessing scheelite as an ore-deposit discriminator using its trace-element and REE chemistry. Can. Mineral. 56, 265–302.
Raimbault, L., Baumer, A., Dubru, M., Benkerrou, C., Croze, V., Zahm, A., 1993. REE fractionation between scheelite and apatite in hydrothermal conditions. Am. Mineral. 78, 1275–1285.
Richards, A., Argles, T., Harris, N., Parrish, R., Ahmad, T., Darbyshire, F., Draganits, E., 2005. Himalayan architecture constrained by isotopic tracers from clastic sediments. Earth Planet. Sci. Lett. 236 (3-4), 773–796.
Shannon, R.D., 1976. Revised effective ionic radii and systematic studies of interatomic distances in halides and chalcogenides. Acta Cryst. 32 (5), 751–767.
Song, G., Cook, N.J., Li, G., Qin, K., Ciobanu, C.L., Yang, Y., Xu, Y., 2019. Scheelite geochemistry in porphyry-skarn W-Mo systems: a case study from the Gaojiabang Deposit. East China. Ore Geol. Rev. 113, 103084. https://doi.org/10.1016/j.oregeorev.2019.103084.
Song, G., Qin, K., Li, G., Evans, N.J., Chen, L., 2014. Scheelite elemental and isotopic signatures: implications for the genesis of skarn-type W-Mo deposits in the Chizhou Area, Anhui Province, Eastern China. Am. Mineral. 99 (2-3), 303–317.
Steiger, R.H., Jäger, E., 1977. Subcommission on geochronology: convention on the use of decay constants in geo- and cosmochronology. Earth Planet. Sci. Lett. 36 (3), 359–362.
Sun, K.K., Chen, B., 2017. Trace elements and Sr-Nd isotopes of scheelite: implications for the W-Cu-Mo polymetallic mineralization of the Shimensi deposit, South China. Am. Mineral. 102, 1114–1128.
Sun, K., Chen, B., Deng, J., 2019. Ore genesis of the Zhuxi supergiant W-Cu skarn polymetallic deposit, South China: evidence from scheelite geochemistry. Ore Geol. Rev. 107, 14–29.
Sun, S.-s., McDonough, W.F., 1989. Chemical and isotopic systematics of oceanic basalts: implications for mantle composition and processes. Geol. Soc. Lond. Spec. Publ. 42 (1), 313–345.
Sun, X., Zheng, Y., Wang, C., Zhao, Z., Geng, X., 2016a. Identifying geochemical anomalies associated with Sb-Au-Pb-Zn-Ag mineralization in north Himalaya, southern Tibet. Ore Geol. Rev. 73, 1–12.
Sun, X., Wei, H., Zhai, W., Shi, G., Liang, Y., Mo, R., Han, M., Yi, J., Zhang, X., 2016b. Fluid inclusion geochemistry and Ar-Ar geochronology of the Cenozoic Bangbu orogenic gold deposit, southern Tibet. China. Ore Geol. Rev. 74, 196–210.
Tyson, R.M., Hemphill, W.R., Theisen, A.F., 1988. Effect of the W: Mo ratio on the shift of excitation and emission spectra in the scheelite-powellite series. Am. Mineral. 73, 1145–1154.
Wagner, T., Boyce, A.J., 2006. Pyrite metamorphism in the Devonian Hunsrück Slate of Germany: insights from laser microprobe sulfur isotope analysis and thermodynamic modeling. Am. J. Sci. 306, 525–552.
Wang, R.C., Wu, F.Y., Xie, L., Liu, X.C., Wang, J.M., Yang, L., Lai, W., Liu, C., 2017. A preliminary study of rare-metal mineralization in the Himalayan leucogranite belts. South Tibet. Sci. China Earth Sci. 60 (9), 1655–1663.
Wissink, G.K., Hoke, G.D., Garzione, C.N., Liu-Zeng, J., 2016. Temporal and spatial patterns of sediment routing across the southeast margin of the Tibetan Plateau: insights from detrital zircon. Tectonics 35 (11), 2538–2563.
Wu, F.-Y., Liu, X.-C., Liu, Z.-C., Wang, R.-C., Xie, L., Wang, J.-M., Ji, W.-Q., Yang, L., Liu, C., Khanal, G.P., He, S.-X., 2020. Highly fractionated Himalayan leucogranites and associated rare-metal mineralization. Lithos 352-353, 105319. https://doi.org/10.1016/j.lithos.2019.105319.
Wu, F., Liu, Z., Liu, X., Ji, W., 2015. Himalayan leucogranite: petrogenesis and implications to orogenesis and plateau uplift. Acta Petrol. Sin. 31, 1–36 (in Chinese with English abstract).
Xia, X.B., Xiang, A.P., Li, G.M., Zhang, L.K., Cao, H.W., Zhang, Z., Liang, W., 2019. Neoproterozoic magmatism of Cuonadong dome and its tectonic implication, Tibet, China. J. Chengdu Univ. Technol. (Sci. Technol. Ed.) 46, 435–448 (in Chinese with English abstract).
Xiang, A., Li, W., Li, G., Dai, Z., Yu, H., Yang, F., 2020. Mineralogy, isotope geochemistry and ore genesis of the miocene Cuonadong leucogranite-related Be-W-Sn skarn deposit in Southern Tibet. J. Asian Earth Sci. 196, 104358. https://doi.org/10.1016/j.jseaes.2020.104358.
Xie, J., Qiu, H., Bai, X., Zhang, W., Wang, Q., Xia, X., 2018. Geochronological and geochemical constraints on the Cuonadong leucogranite, eastern Himalaya. Acta Geochim. 37 (3), 347–359.
Xie, L., Tao, X., Wang, R., Wu, F., Liu, C., Liu, X., Li, X., Zhang, R., 2020. Highly fractionated leucogranites in the eastern Himalayan Cuonadong dome and related magmatic Be-Nb-Ta and hydrothermal Be-W-Sn mineralization. Lithos 354-355, 105286. https://doi.org/10.1016/j.lithos.2019.105286.
Yang, Z., Hou, Z., Meng, X., Liu, Y., Fei, H., Tian, S., Li, Z., Gao, W., 2009. Post-collisional Sb and Au mineralization related to the South Tibetan detachment system, Himalayan orogen. Ore Geol. Rev. 36 (1-3), 194–212.
Yin, A.n., 2006. Cenozoic tectonic evolution of the Himalayan orogen as constrained by along-strike variation of structural geometry, exhumation history, and foreland sedimentation. Earth-Sci. Rev. 76 (1-2), 1–131.
Yin, A.n., Harrison, T.M., 2000. Geologic evolution of the Himalayan-Tibetan orogen. Annu. Rev. Earth Planet. Sci. 28 (1), 211–280.
Yuan, L., Chi, G., Wang, M., Li, Z., Xu, D., Deng, T., Geng, J., Hu, M., Zhang, L., 2019. Characteristics of REEs and trace elements in scheelite from the Zhuxi W deposit, South China: implications for the ore-forming conditions and processes. Ore Geol. Rev. 109, 585–597.
Zaw, K., 2000. Formation of magnetite-scheelite skarn mineralization at kara, northwestern tasmania: evidence from mineral chemistry and stable isotopes. Econ. Geol. 95, 1215-1230.
Zeng, L.-P., Zhao, X.-F., Hammerli, J., Fan, T.-W.-T., Spandler, C., 2020. Tracking fluid sources for skarn formation using scapolite geochemistry: an example from the Jinshandian iron skarn deposit, Eastern China. Miner. Deposita. 55 (5), 1029–1046.
Zeng, L., Gao, L.-E., Dong, C., Tang, S., 2012. High-pressure melting of metapelite and the formation of Ca-rich granitic melts in the Namche Barwa Massif, southern Tibet. Gondwana Res. 21 (1), 138–151.
Zeng, L., Gao, L.-E., Tang, S., Hou, K., Guo, C., Hu, G., 2015. Eocene magmatism in the Tethyan Himalaya, southern Tibet. Geol. Soc. Lond. Spec. Publ. 412 (1), 287–316.
Zeng, L., Gao, L.-E., Xie, K., Liu-Zeng, J., 2011. Mid-Eocene high Sr/Y granites in the Northern Himalayan Gneiss Domes: melting thickened lower continental crust. Earth Planet. Sci. Lett. 303 (3-4), 251–266.
Zeng, L.S., Liu, J., Gao, L., Xie, K.J., Wen, L.i., 2009. Early Oligocene anatexis in the Yardoi gneiss dome, southern Tibet and geological implications. Chinese Sci. Bull. 54 (1), 104–112.
Zhang, J.J., Guo, L., Zhang, B., 2007. Structure and kinematics of the Yalashangbo dome in the northern Himalayan dome belt. China. Chin. J. Geol. 42, 16–30 (in Chinese with English abstract).
Zhang, J., Santosh, M., Wang, X., Guo, L., Yang, X., Zhang, B.o., 2012. Tectonics of the northern Himalaya since the India-Asia collision. Gondwana Res. 21 (4), 939–960.
Zhang, L.-K., Li, G.-M., Cao, H.-W., Zhang, Z., Dong, S.-L., Liang, W., Fu, J.-G., Huang, Y., Xia, X.-B., Dai, Z.-W., Pei, Q.-M., Zhang, S.-T., 2020a. Activity of the south Tibetan detachment system: constraints from leucogranite ages in the eastern Himalayas. Geol. J. 55 (7), 5540–5573.
Zhang, L.K., Li, G.M., Santosh, M., Cao, H.W., Dong, S.L., Zhang, Z., Fu, J.G., Xia, X.B., Huang, Y., Liang, W., Zhang, S.T., Li, S., 2019. Cambrian magmatism in the Tethys Himalaya and implications for the evolution of the Proto-Tethys along the northern Gondwana margin: a case study and overview. Geol. J. 54 (4), 2545–2565.
Zhang, L.K., Zhang, Z., Li, G.M., Dong, S.L., Xia, X.B., Liang, W., Cao, H.W., 2018a. Rock assemblage, structural characteristics and genesis mechanism of the Cuonadong Dome, Tethys Himalaya. Earth Sci. 43, 2664–2683 (in Chinese with English abstract).
Zhang, Q., Zhang, R.Q., Gao, J.F., Lu, J.J., Wu, J.W., 2018b. In-situ LA-ICP-MS trace elemental analyses of scheelite and wolframite: constraints on the genesis of veinlet-disseminated and vein-type tungsten deposits, South China. Ore Geol. Rev. 99, 166–179.
Zhang, Y.-X., Zhang, K.-J., 2017. Early Permian Qiangtang flood basalts, northern Tibet, China: a mantle plume that disintegrated northern Gondwana? Gondwana Res. 44, 96–108.
Zhang, Z., Li, G.M., Zhang, L.K., Qing, C.S., Huang, Y., Liang, W., Cao, H.W., Wang, Y.Y., Dong, S.L., Lu, L., Dai, Z.W., 2020b. Genesis of the Mingsai Au deposit, southern Tibet: Constraints from geology, fluid inclusions, $^{40}Ar/^{39}Ar$ geochronology, H-O isotopes, and in situ sulfur isotope compositions of pyrite. Ore Geol. Rev. 122, 1–16.
Zhao, W.W., Zhou, M.-F., Williams-Jones, A.E., Zhao, Z., 2018. Constraints on the uptake of REE by scheelite in the Baoshan tungsten skarn deposit, South China. Chem. Geol. 477, 123–136.
Zheng, Y.F., Wu, F.Y., 2018. The timing of continental collision between Indian and Asia. Sci. Bull. 63, 1649–1654.
Zheng, Y.Y., Sun, X., Tian, L.M., Zheng, H.T., Yu, M., Yang, W.T., Zhou, T.C., Geng, X.B., 2014. Mineralization, deposit type and metallogenic age of the gold antimony polymetallic belt in the eastern part of North Himalayan. Geotect. Metall. 38, 108–118 (in Chinese with English abstract).